Exploring Impacts of Differing Aerosol Environments on Radar Signatures of Deep Convection near Houston, Texas, using a Bulk Statistical Framework

JONAH PEHL,[a,c] GREG MCFARQUHAR,[a,c] JEFFREY SNYDER,[b] AND JASON FURTADO[c]

[a] *Cooperative Institute for Severe and High-Impact Weather Research and Operations, Norman, Oklahoma*
[b] *NOAA/OAR/National Severe Storms Laboratory, Norman, Oklahoma*
[c] *School of Meteorology, The University of Oklahoma, Norman, Oklahoma*

(Manuscript received 16 January 2024, in final form 15 November 2024, accepted 12 December 2024)

ABSTRACT: Aerosol deep-convective cloud (DCC) interactions remain highly uncertain in the study of water cycles, energy budgets, climate projections, and air quality, partly because it is difficult to disentangle aerosol impacts from the impacts of meteorology in observational studies. Prior studies have shown that increased aerosol ingestion by DCC updrafts can influence their microphysical characteristics through the mixed-phase and condensational aerosol invigoration effects. However, other studies claim that increased aerosol loading produces different microphysical responses that are not consistent with invigoration. This study thus examines the impact of aerosol regimes on DCC microphysics by analyzing ~1300 DCCs tracked from the Houston–Galveston WSR-88D. Fields from the fifth major global reanalysis produced by ECMWF and Modern-Era Retrospective Analysis for Research and Applications, version 2, are used to estimate meteorological and aerosol conditions near DCCs. DCC tracking was completed using the Multicell Identification and Tracking algorithm applied to radar data. Composite difference contoured frequency by altitude diagrams show statistically significant bulk differences in the vertical structure of dual-polarization radar data that are consistent with previous studies. The probabilistic differences in radar variables were typically 1%–6% above the freezing level and <4% below the freezing level. Microphysical fingerprint distributions showed that DCCs under high aerosol loading exhibit decreased warm rain, increased freezing rates, and increased vapor deposition onto ice. These signatures together are found to be consistent with increased aerosol loading leading to less warm rain, more evaporation under high tropospheric moisture conditions leading to less cold rain, and increased riming/accretion in environments with large instability leading to more cold rain.

KEYWORDS: Deep convection; Aerosols; Cloud microphysics; Radars/Radar observations; Statistics

1. Introduction

Aerosols emitted into Earth's atmosphere provide the particles necessary for the condensation of water vapor to occur at relative humidities just above saturation, with these particles known as cloud condensation nuclei (CCNs) (Köhler 1921). Given aerosol prevalence across the globe and their effects on the changing climate system due to increasing anthropogenic activities, the importance of understanding their impacts on water and energy budgets through cloud interactions is a priority for understanding how climate may change in the future (IPCC 2023). However, due to the difficulty in separating meteorological and aerosol influences in observational studies (e.g., Varble 2018; Grabowski 2018; Zamora and Kahn 2020; Varble et al. 2023), aerosols' influence on all types of clouds remains poorly known, especially within isolated deep-convective clouds (DCCs).

Broadly, the aerosol indirect effects on clouds can be separated into the first (Twomey 1977) and second (Albrecht 1989) indirect effects. The first indirect effect explains how increased aerosol concentration, and thus CCN, leads to an increased cloud albedo due to more surface area available for scattering from more numerous but smaller droplets. The second indirect effect describes how increased CCN concentration ingestion by updrafts can lead to narrower drop size distributions (DSDs) from the increase in competition for condensate which inhibits the warm rain processes. There are many theories regarding aerosol impacts on DCCs in regards to updraft invigoration, and thus microphysical and precipitation changes, through the second indirect effect. One such theory is the *mixed-phase* (or *cold-phase*) aerosol invigoration effect (MAIE) which has been hypothesized to act in DCCs that precipitate and whose updrafts reach above the environmental freezing level (EFL) (Andreae et al. 2004; Rosenfeld et al. 2008). It is theorized that the decrease in warm rain leads to increased transport of liquid mass to the freezing level leading to increased freezing and riming rates that release more latent heat, further increasing updraft buoyancy and vertical velocity. The MAIE mechanism differs from other recently introduced aerosol invigoration mechanisms such as *condensational* invigoration described by Khain et al. (2012), Fan et al. (2018), Cotton and Walko (2021), Khain et al. (2022), and Zang et al. (2023). This theory describes how the increased surface area of the more numerous but smaller droplets in the liquid or mixed phase increases vapor deposition rates onto the droplets, increasing net latent heat release via condensation. While it is extremely difficult to affirm convective invigoration in an observational study such as this, it is possible to quantify resulting microphysical responses and state whether they are consistent with proposed invigoration theories.

Following Rosenfeld et al. (2008), many studies have attempted to support or question aerosol effects on DCC microphysical responses in different meteorological environments

Corresponding author: Jonah Pehl, jonah.pehl@ou.edu

DOI: 10.1175/JAS-D-24-0008.1

through modeling and observational methods. In situ observational studies that have found evidence of microphysical responses in DCCs point to the narrowing of DSDs (Rosenfeld and Lensky 1998) and a reduction in cloud droplet effective radius in the presence of high aerosol loading at temperatures above and well below 0°C, consistent with the MAIE theory (e.g., Rosenfeld and Woodley 2000; Andreae et al. 2004; Matsui et al. 2004; Koren et al. 2005). Further, due to narrower DSDs with smaller cloud droplets within the warm region, Sherwood (2002), Sherwood et al. (2006), and Lindsey and Fromm (2008) all showed smaller ice particles above the freezing level with increased aerosol loading. Increased number concentrations of supercooled drops have also been observed in continental aerosol regimes (higher aerosol number concentrations) compared to maritime regimes (lower aerosol number concentrations) by Rosenfeld and Woodley (2000). Further, Williams et al. (1999) and Rosenfeld and Woodley (2000) found that precipitation formation could be delayed to altitudes well above the freezing level. However, the impacts of aerosol loading on the total amount of precipitation observed at the surface are less clear. Huang et al. (2009) found that aerosols reduced the amount of total precipitation in agreement with studies conducted by Givati and Rosenfeld (2004) and Jirak and Cotton (2006), but Bell et al. (2008), Li et al. (2011), and Koren et al. (2012) showed larger accumulations of precipitation in mixed-phase clouds under high aerosol loading. Additionally, the consistent feature of decreased frequency of light rain and increased frequency of heavy rain from aerosol loading effects has been documented by numerous studies (e.g., Qian et al. 2009; Li et al. 2011; Fan et al. 2013, 2016). The uncertainty in the impact of aerosol loading on precipitation accumulation can be attributed to the complex nature of thermodynamic and microphysical feedbacks that occur in deep mixed-phase convection as well as the ability of further convection to be triggered from cold pools (e.g., Khain 2009). Freezing processes occurring within the mixed-phase region of DCCs are highly sensitive not only to the number of cloud droplets being transported above the freezing level but also to the number concentrations of ice-nucleating particles, humidity, instability, and wind shear. These effects, however, are difficult to disentangle in observational studies alone as pointed out by Varble (2018), Veals et al. (2022), and Varble et al. (2023). These studies argue that attribution of microphysical responses, precipitation changes, and possible convective invigoration by increased aerosol concentration is extremely difficult to do given the complex microphysical/dynamic coupling that occurs and the inability to adequately constrain for meteorological influences.

Modeling studies that examine the influences of aerosols on DCCs may be able to better attribute causality of aerosol impacts rather than the correlations noted in observations due to the ability to examine impacts from a single property or process. However, the simulations must be evaluated against observations to determine whether they are representative of natural clouds as needed to evaluate hypotheses on the role of specific processes. For example, Khain et al. (2005) and Fan et al. (2009) conducted aerosol/DCC interaction simulations, finding that the effects of increased aerosol loading on DCCs can be consistent with invigoration, given moderate instability and low wind shear conditions. Additionally, Carrió et al. (2010), Lerach and Cotton (2012), and Ilotoviz et al. (2018) explored the consequences of increased CCN ingestion into updrafts on the microphysics and dynamics of a DCC. They found increases in the concentration and sizes of supercooled droplets in the first few kilometers above the freezing level which enhanced the wet growth of hail allowing it to reach very large sizes. In the low CCN concentration cases, the accretion of supercooled droplets onto hail and freezing drops was extremely inefficient, which caused decreased differential reflectivity (Z_{DR}) within the Z_{DR} column. Further, many modeling studies such as Wang (2005), Seifert and Beheng (2006), Fan et al. (2007), Tao et al. (2007), and Li et al. (2009) showed that higher aerosol loading leads to DCCs or convective systems with stronger updrafts, increased latent heat release, and larger concentrations of liquid and frozen particles, which can impact signatures of reflectivity at horizontal polarization (Z_H) and Z_{DR} near and above the freezing level. In contrast, other studies have found conflicting evidence through modeling (e.g., Morrison and Grabowski 2011; Morrison 2012; Boucher and Quaas 2013; Grabowski 2015; Grabowski and Morrison 2016; Grabowski 2018; Grabowski and Morrison 2020; White et al. 2017). Yet, these studies' methods have still been questioned by others such as Fan et al. (2012) and Wang et al. (2013) for using fixed droplet and prescribed aerosol number concentrations that unrealistically simulate droplet number and activation. Also, studies using saturation adjustment neglect the condensational invigoration mechanisms as shown by Lebo et al. (2012), Fan and Khain (2021), and Zhang et al. (2021). These discrepancies show inherent limitations of modeling with potential biases depending on the microphysical schemes, initialized data, boundary conditions, resolution, and other parameterizations, such as those of the boundary layer, used (White et al. 2017; Varble et al. 2023).

This study seeks to uncover which theories provided by previous work are consistent with the observed bulk differences in microphysical properties within DCCs under differing aerosol number concentrations. The area surrounding Houston, Texas, provides an adequate natural laboratory to investigate these issues due to regular DCC occurrence, greatly differing concentrations of aerosols, and general lack of other meteorological influences during the summer months (JJA). Other studies conducted within the Houston/Gulf of America (formerly Gulf of Mexico) area have generally found that DCCs can exhibit enhanced precipitation, delayed warm rain processes, stronger vertical velocities in updrafts, and increased lightning rates when under high aerosol loading (e.g., Shepherd and Burian 2003; Fan et al. 2007, 2020; Hu et al. 2019a; Marinescu et al. 2021; Zhang et al. 2021). However, the overarching microphysical properties of DCCs have yet to be quantified under differing aerosol loading regimes. Therefore, the following questions are addressed in this work:

1) What are the aerosol effects on the bulk statistical properties of polarimetric radar data?
2) Are the bulk effects of aerosols consistent with previous theories regarding precipitation and relevant microphysical processes?

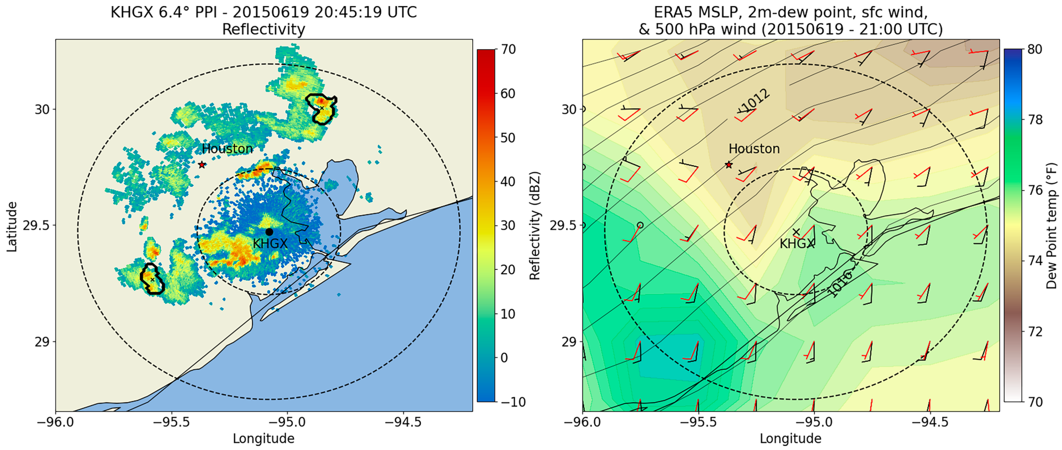

FIG. 1. (left) Radar reflectivity Z_H from the 6.4° PPI scan conducted by KHGX at 2045:19 UTC 19 Jun 2015 with overlaid DCC areal boundaries (black lines) and centroids (denoted by "x") identified by MCIT. (right) Mean sea level pressure (MSLP; hPa) (thin black contours), 2-m dewpoint temperature (°F) (shaded), surface wind [knots (kt; 1 kt ≈ 0.51 m s^{-1})] (black barbs), and 500-hPa wind (kt) (red barbs) at every ERA5 grid point around KHGX at 2100 UTC 19 Jun 2015. Range rings (dashed circles) are plotted for the domain used in the study (30–80 km from KHGX).

3) Do meteorological influences mediate the aerosol effects as stated by previous work?

The remainder of this article is organized as follows. Section 2 presents the bulk statistical framework used to investigate aerosol impacts on convective cloud properties. Section 3 presents results found from the statistical analysis and interprets those results. Section 4 presents important conclusions regarding aerosol effects on convective clouds, shows the limitations of those results, and offers suggestions for future research.

2. Data and methods

a. Case selection

In general, studies that reinforce the capability of aerosols to affect DCCs have found that the effects are moderated by three main meteorological variables: relative humidity (RH) throughout the depth of the troposphere, instability, and wind shear (e.g., Khain et al. 2008; Fan et al. 2009; Khain 2009; Koren et al. 2010; Tao et al. 2012; Altaratz et al. 2014; Dagan et al. 2015; Peters et al. 2023). In brief, humid environments with weak wind shear and moderate instability have been theorized to greatly foster aerosol invigoration for mixed-phase convection because the DCCs are better able to withstand entrainment at the cloud periphery (Dagan et al. 2015). Additionally, they have high precipitation efficiency due to the lack of strong shear and the presence of instability to loft condensate mass to the freezing level in the presence of increased aerosol loading (Khain et al. 2008; Altaratz et al. 2014). It is these types of environments that lead to the selection of the southeast Texas region for this study so that aerosol effects can be better unmasked. While a plethora of convective environments occur within the southeast Texas region in the summer season, warm-season mesoscale sea-breeze circulations are the focus of this study. Other synoptic-scale phenomena such as cold fronts, extratropical cyclones, and hurricanes, or intense mesoscale boundaries that may be strongly baroclinic such as outflows, often provide stronger forcing on the DCCs. These can increase the difficulty in disentangling aerosol and meteorological impacts because they can cause differing modes of convection that can dominate vertical microphysical structure and impact aerosol/CCN transport within the boundary layer (e.g., Varble 2018).

Manual case selection was completed by observing the meteorological environments from the observed upper-air charts, radar reflectivity evolution around Houston, Texas, and surface METAR station evolution. Each day in the months of June, July, and August from the years 2013–21 was analyzed, and a day was chosen for subsequent analysis based on whether isolated convective cells formed within the scanning volume of the KHGX WSR-88D in a sea-breeze environment. Additionally, if any synoptic-scale cold fronts, hurricanes, or outflow boundaries passed over the Houston area the day before, that day was not selected for further analysis. This was done to ensure that wind influences on aerosol transport, which could lead to large differences in the chemical composition of CCN populations (e.g., Levy et al. 2013), and meteorological conditions would remain as similar as possible. This yielded a total of 219 case days to use for subsequent analysis (Fig. B1 in appendix B). Figure 1 shows an example of a typical meteorological environment chosen for this study in which there was clear onshore surface flow throughout the morning and afternoon that triggered isolated DCCs near KHGX in a regime characterized by weak synoptic forcing.

b. KHGX WSR-88D

DCCs in this study were sampled using KHGX, a WSR-88D operational radar located near Houston, Texas. KHGX was upgraded to dual polarization in early 2013, which hence marks the earliest period for which the data can be used. The radar is located in Galveston County, Texas, at an elevation of 35 m and provides radar coverage of the entire southeast

Texas region and northwestern regions of the Gulf Coast. The NEXRAD volume coverage patterns (VCPs) utilized in this study are from various precipitation modes (VCP 11, VCP 21, VCP 211, VCP 121, VCP 212, and VCP 12) and clear air modes (VCP 32 and VCP 35) [National Research Council (NRC) 2002]. For analysis, radar gates with copolar correlation coefficient (ρ_{hv}) below 0.8 and Z_H below −10 dBZ were removed because they likely represented nonmeteorological scatterers and low signal-to-noise ratios.

c. The MCIT algorithm

The Multicell Identification and Tracking (MCIT) algorithm was developed for use in operational applications to objectively identify and track individual convective cells using radar data (Hu et al. 2019b). A detailed overview of the MCIT and the parameters within is given by Hu et al. (2019b). Briefly, MCIT uses level-2 radar data from all elevation angles within a volume scan, data from lighting map arrays, and data from the National Lightning Detection Network to track DCCs' spatial extent (X, Y, and Z coordinates relative to the radar of interest) on a volumetric update time scale (about every 5 min). It computes centroids based on their identified areal boundaries from a watershed algorithm and handles merging/splitting based on thresholds prescribed by the user. For this study, MCIT was used to objectively track DCCs in space and time across the 219 case days. Further processing was conducted to minimize spurious identification of cells. To be used in the analysis, each DCC must have existed for at least six MCIT time steps/volume scans (about 30 min) and occur within a range of 30–80 km from KHGX for its entire lifetime. These ranges were chosen to preserve the vertical resolution of radar data at larger distances from KHGX and to ensure an accurate calculation of echo top height (ETH), which is discussed in section 2e. Additionally, any DCCs that were identified as produced from merging/splitting were not used in the analysis. A map illustrating where DCCs were sampled is shown in appendix B (Fig. B2). Due to the large computational time required by the algorithm to process all case days, sensitivity tests for changing certain parameters that affect cell merging/splitting and minimum cell size/intensity in the algorithm were not performed. This omission most likely does not affect the overall conclusions since most isolated single-cell DCCs investigated here are not merging or connected together like mesoscale convective or multicell systems, for which the choice of these parameters may have a greater impact. The MCIT provides an objective and efficient way of tracking the many DCCs observed near Houston and allows for the creation of a large database containing the individual DCCs along with their centroid locations, time series, and areal boundaries.

d. CFADs and MPS plots

Contoured frequency by altitude diagrams (CFADs) give the vertical variability of normalized histograms of radar returns without providing information on horizontal variability (Yuter and Houze 1995). Here, "aggregate" CFADs are presented where radar data from all DCCs in subsets selected by environmental conditions (e.g., all DCCs over land) are used to calculate the normalized histogram at each altitude, an example of which is shown in Fig. 2 (left column). The y axis is the altitude relative to the freezing level (z), where the freezing level is determined by the fifth major global reanalysis produced by ECMWF (ERA5) reanalysis for each DCC at each time of its existence. This provides an important reference altitude for all DCCs to be compared with each other. Bins of 0.5 km are used in the vertical; for CFADs of Z_H, the x axis is binned every 2 dBZ, and for CFADs of Z_{DR}, the x axis is binned every 0.25 dB.

In many of the single DCC CFADs like that shown in Fig. 2 (upper right), a jump in Z_H can be observed in the upper levels of the cloud. In Fig. 2b, this jump exists in the 6–7-km layer and is caused by the radar beam not sampling as many gates in this altitude range due to the VCP; thus, the trend of decreasing Z_H with altitude is not well captured. Additionally, a second peak is captured in the 0–15-dBZ range in the −4- to −2-km range in Fig. 2a, which is likely caused by many frequent observations of low Z_H due to small hydrometeor concentrations, and is associated with updrafts (e.g., Yuter and Houze 1995).

The composite difference between two aggregate CFADs allows for a direct comparison of the probability of specific radar values occurring at given altitudes, which produces plots similar to those presented by Matsui et al. (2020). In this study, composite differences between aggregate CFADs of DCCs with high and low anthropogenic (A) $PM_{2.5}$ mass concentrations are examined. A discussion regarding the definition of high and low A $PM_{2.5}$ DCCs is presented in section 2g.

Kumjian et al. (2022) describe how different microphysical processes affect the vertical structure of Z_H and Z_{DR} below the freezing level. The vertical gradients in Z_H and Z_{DR} (i.e., ΔZ and ΔZ_{DR}) as plotted on a two-dimensional ΔZ and ΔZ_{DR} plot allow us to infer that different microphysical processes may be dominant (Fig. 3). Kumjian et al. (2022) derive the calculation of ΔZ and ΔZ_{DR} using relatively horizontally homogeneous precipitation events (e.g., spatially broad stratiform precipitation and large-scale tropical cyclones), for which one can use the quasivertical precipitation (QVP) profiles introduced by Ryzhkov et al. (2016). We cannot make use of QVPs for the DCCs used within this study because their spatiotemporal scales are too small for accurate QVP retrievals, necessitating a different method of estimating ΔZ and ΔZ_{DR}. The terms ΔZ and ΔZ_{DR} for this study were calculated for each individual DCC by first determining the median of the normalized histogram at each altitude bin. A linear best fit is applied to the median values of radar data as a function of altitude; an example of the resultant slope is shown in Fig. 2b. The reciprocal of this slope gives a slope of dBZ per kilometer and is defined such that a positive slope indicates an increase in radar data value toward the ground, as defined by Kumjian et al. (2022). Then, ΔZ and ΔZ_{DR} pairs for each DCC are plotted on the microphysical parameter space (MPS), a 2D Gaussian kernel density estimate (KDE) is computed from these points using the "Scott" bandwidth method (Scott 2015), and each kernel density estimate can be subtracted from an estimate of another subset of DCCs, to get the difference in probability normalized by sample sizes of where DCCs are likely to occur in the MPS. This technique was completed for three vertical sections of the CFAD,

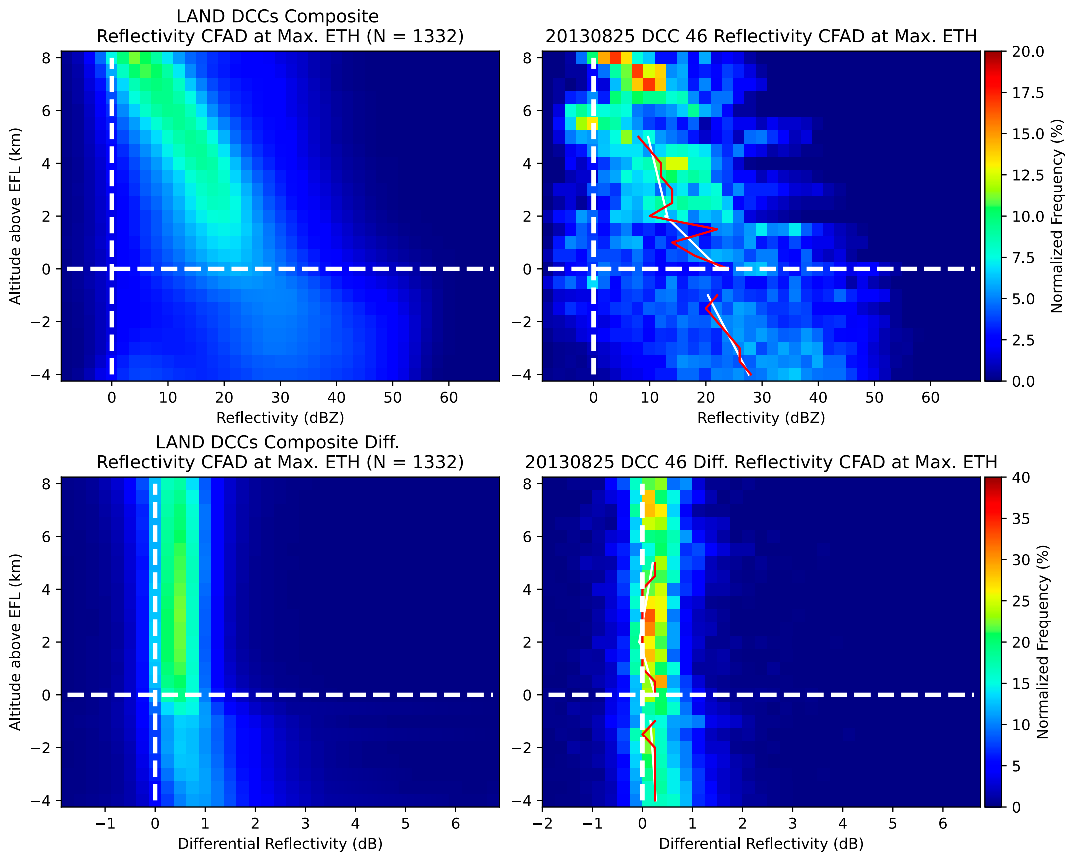

FIG. 2. (left) Aggregate CFADs for all cells over land ($N = 1332$) and (right) CFADs for cell 46 on 25 Aug 2013 at the time of maximum ETH achieved by the DCCs. (right) The red line refers to the median values of radar data at each altitude bin and the white line is the least squares best fit for those points.

-4 km $\le z \le -1$ km (i.e., below the freezing level), 0 km $\le z \le 2$ km (i.e., in the Z_{DR} column region), and 2 km $\le z \le 5$ km (i.e., above the typical Z_{DR} column) (Fig. 2, right column). Each area is chosen so that inferences about microphysical fingerprints for liquid, mixed-phase, and cold-phase processes can be made. Overall, the use of the MPS plots given by ΔZ and ΔZ_{DR} here is meant only to supplement and aid the interpretation of the composite difference CFADs.

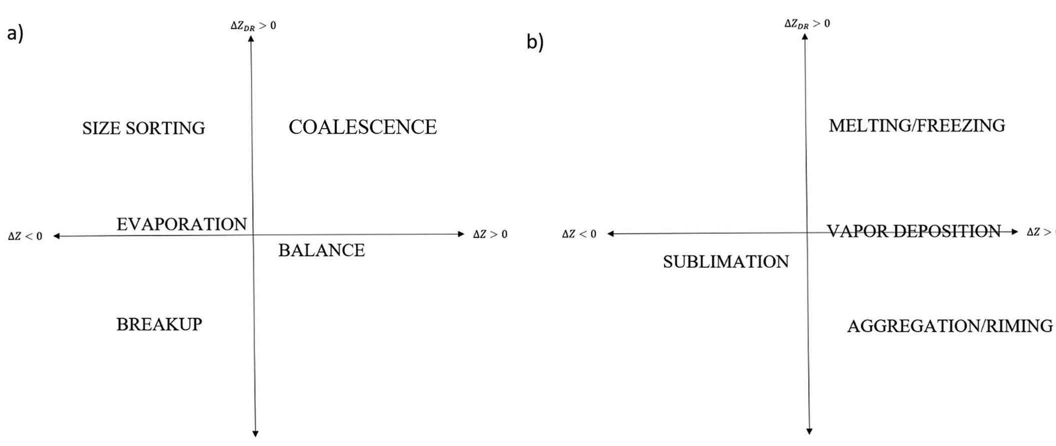

FIG. 3. The parameter space of ΔZ and ΔZ_{DR} with (a) important microphysical processes in liquid and (b) mixed-phase/cold-phase precipitation inferred from signs of ΔZ and ΔZ_{DR}. Adapted from Kumjian et al. (2022).

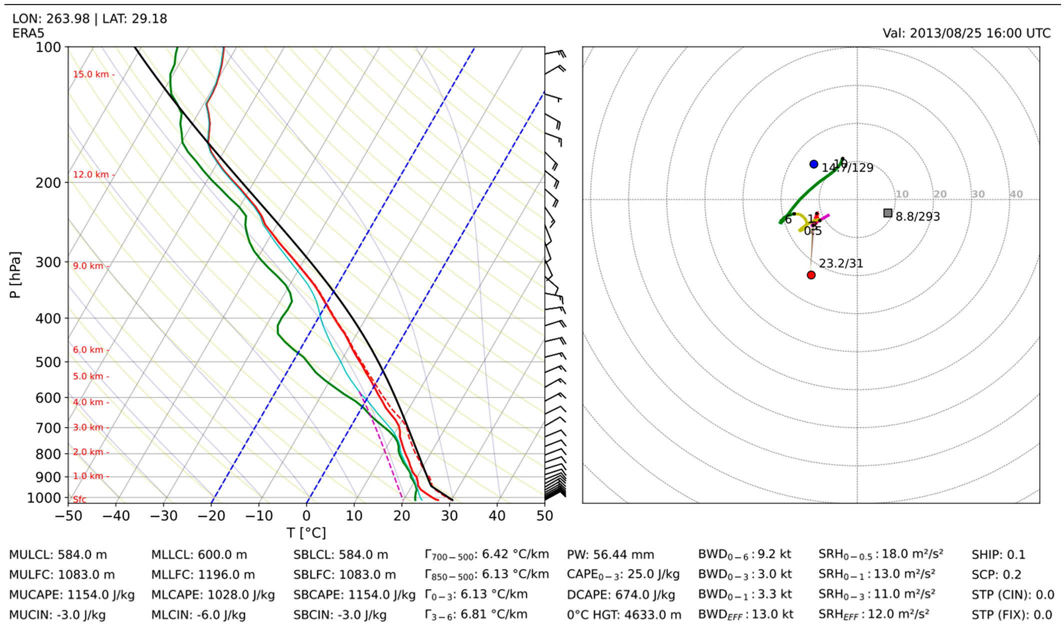

FIG. 4. Example sounding reconstructed from the ERA5 reanalysis for DCC 46 at 1600 UTC 25 Aug 2013.

e. *Echo top height*

To ensure a consistent comparison of DCCs with the CFADs and MPS plots, DCCs need to be analyzed at similar times in their life cycle. Therefore, ETHs are used to proxy updraft maturity. ETHs have been used for decades (e.g., Held 1978; Evans et al. 2004, among others) in operational settings and have been shown to temporally correlate with changes in cloud-top height and peak updraft intensity (Dworak et al. 2012; Bluestein et al. 2019). The use of ETH here is to identify the time at which each DCC reaches peak intensity to ensure DCCs are being compared at similar stages of their life cycle; thus, all radar data shown are from the DCC's time of peak ETH.

Typically, ETH is computed by retrieving the highest elevation scan in which at least an 18-dB*Z* echo is returned (Donaldson 1964; Lakshmanan et al. 2013). Height is then calculated using a 4/3 Earth model to account for standard atmospheric refraction of the radar beam (Doviak et al. 1994). The half-power beamwidth above the nominal elevation angle is used to account for the vertical extent of the beam. However, Lakshmanan et al. (2013) proposed a slight change in methodology for calculating ETH to improve accuracy. This change interpolates the ETH based on the elevation scans that bracket the threshold of 18 dB*Z* and is the technique used in this study. Additionally, a minimum ETH of 3 km above the freezing level was set for DCCs to be included in this study to ensure they likely contained ice. Distributions of DCC initiation times relative to the diurnal cycle, MCIT lifetimes, and maximum ETHs are shown in appendix B (Fig. B3) to illustrate the typical DCC sampled in this study.

f. *Meteorological dataset*

The meteorological fields were determined using the ERA5 reanalysis which has a 31-km grid spacing in the horizontal, 137 vertical pressure levels, and hourly temporal output (Hersbach et al. 2020). To characterize the meteorological environment, vertical soundings were reconstructed from the ERA5 data at the nearest spatiotemporal grid point to each DCC initiation time in the MCIT algorithm (an example is shown in Fig. 4). Variables to analyze from the soundings were collected to separate meteorological and aerosol effects and test the hypotheses that aerosol impacts are largely dependent on tropospheric humidity, instability, and shear (Table 1). It should be noted that instability can be characterized by parcel parameters such as CAPE and equilibrium level (EL). In this study, it was found that most unstable CAPE (MUCAPE) and EL showed similar correlations with the radar data distributions, and thus, EL was chosen to be omitted from the analysis.

Correlation analysis is used to understand how the characteristics of the radar variable distributions as a function of altitude are correlated with the meteorological variables extracted from the ERA5 soundings. This is important as the characteristics of the radar variable distributions, such as central tendency and standard deviation, are what the CFADs display, and meteorological impacts on these need to be controlled for to uncover

TABLE 1. ERA5 meteorological variables sampled near DCCs and their altitudes relative to the freezing level.

Variable	Altitude relative to freezing level (km)
RH	−3.5, −3, −2.5, −2, −1.5, −1, −0.5, 0, 0.5, 1, 1.5, 2, 2.5, 3, 3.5, 4, 4.5, 5, 5.5, 6, 6.5, 7, 7.5, 8
PW	Column
MUCAPE	Column
BWD 0–9 km (BWD09)	Column
DCAPE	Column

any aerosol effects. For correlation analysis, the median and standard deviation of each histogram at each altitude bin are correlated with each meteorological variable for Z_H and Z_{DR} for each DCC at the time of their maximum ETH.

g. *Aerosol dataset*

Over the Houston region, there is a lack of observations of explicit CCN size distributions near DCCs for the time and spatial scales this study uses. Thus, in this study, the surface mass concentration of $PM_{2.5}$ is used as a proxy to quantify the loading of common-sized CCN particles. Although in general increased air pollution leads to increased CCN number concentrations (e.g., Lance et al. 2009; Duan et al. 2018), this relationship is not linear. This is because the number of CCN that can activate under a given supersaturation can be highly variable since not all particles, even within the $PM_{2.5}$ size range, are equally effective at activating. For example, Duan et al. (2018) reported in the Guangzhou region that a general elevation of CCN number concentration occurred with increased $PM_{2.5}$ mass concentration but was not easily predicted. It is recognized that $PM_{2.5}$ mass concentration is not an ideal proxy for CCN number concentration and is incapable of always accounting for the complex processes of CCN activation. However, other studies which use imperfect aerosol proxies such as $PM_{2.5}$ mass concentration to deduce aerosol impacts (e.g., Fuchs et al. 2015; Chen et al. 2021) show that these data are viable for estimating general periods of high and low CCN number concentrations. Further, the availability of these data for the large time period of this study is crucial for constructing a large dataset and inaccuracies in the aerosol proxy are likely averaged out.

The Modern-Era Retrospective Analysis for Research and Applications, version 2 (MERRA-2), reanalysis model is used for determining the $PM_{2.5}$ mass concentration in the vicinity of the DCCs. The MERRA-2 uses a resolution of 0.5° × 0.625° (latitude by longitude) and includes hourly data. Randles et al. (2017) discuss MERRA-2 aerosol assimilation techniques used to calculate mass concentrations of certain aerosol species and describe the calculation of the $PM_{2.5}$ mass concentration as

$$PM_{2.5} = DU_{2.5} + OC + BC + SS_{2.5} + SO_4(132.14/96.06), \quad (1)$$

where $DU_{2.5}$ is the dust, OC is the organic carbon, BC is the black carbon, $SS_{2.5}$ is the sea salt, and SO_4 is the sulfate. These values are evaluated at the surface per the MERRA-2 documentation (Randles et al. 2017). It is assumed that DCCs are surface based or at least that the surface $PM_{2.5}$ adequately quantifies periods in space and time of more pollution within the boundary layer and that DCCs ingest this air.

A quantitative comparison of MERRA-2 $PM_{2.5}$ and Texas Center for Environmental Quality site records was done in the preliminary stages of this work as these sites were a potential candidate for $PM_{2.5}$ data (see Pehl 2023, chapter 3.4). It was found that for most of this study's time frame only a few sites were recording $PM_{2.5}$ and the sampling times were not consistent. Given this, MERRA-2 was chosen to provide an approximation of differing aerosol environments across the many years of this study. The reader is referred to Pehl (2023) for a more in-depth look into the errors associated with MERRA-2's $PM_{2.5}$ approximation in the Houston, Texas, area.

When sampling DCCs, the MERRA-2 $PM_{2.5}$ mass concentration is split into the natural (sea salt and dust) and anthropogenic (organic carbon, black carbon, and sulfate) regimes. For this study, the focus is set on the total $PM_{2.5}$ contributed by the anthropogenic constituents as these are typically more numerous, similar in size, and better related to CCN number concentration/cloud droplet concentration at cloud base than the large, natural constituents (especially when mass concentration is being used) (IPCC 2007; Miller et al. 2023). Note that because $PM_{2.5}$ mass concentration is used, large anthropogenic species are represented more so than ultrafine particles. For the analysis of DCCs in section 3, the *A* $PM_{2.5}$ mass concentration is determined by sampling the nearest spatiotemporal grid point to each DCC initiation in the MCIT algorithm. Classification of DCCs with high and low *A* $PM_{2.5}$ mass concentration is done for each specific subset of data and thus depends on the subsetting techniques. For example, given a distribution of *A* $PM_{2.5}$ mass concentration for all DCCs over land, DCCs with high and low *A* $PM_{2.5}$ are identified using the top and bottom terciles of the land distribution. This method means that the threshold classification of high and low *A* $PM_{2.5}$ mass concentration is not fixed across the entire dataset, but instead is defined within a given meteorological bin based on the upper and lower terciles. This allows for a similar number of DCCs to be in the high and low *A* $PM_{2.5}$ mass concentration classifications when subsetting based on meteorological variables, which leads to a similar significance across high and low aerosol regimes.

It should be noted that MERRA-2 meteorological fields were not considered and instead were supplied by the ERA5 as discussed in section 2f. This is because MERRA-2 does not report hourly meteorological fields at numerous pressure levels like the ERA5 does, which is one reason why the ERA5 is better for sampling convective environments (Taszarek et al. 2021). Additionally, ERA5 does not report aerosol information at the hourly time scale; thus, MERRA-2 was used for aerosol data.

3. Results

a. *Correlation analysis of radar variable distributions*

Figure 5 shows correlations of median and standard deviations for Z_H and Z_{DR} distributions at all altitudes of the CFADs with meteorological variables determined using the ERA5 reanalysis for DCCs over land.

In general, characteristics of the Z_H distributions (Figs. 5a,b) are negatively correlated with RH near and below the freezing level. Meanwhile, the median of the Z_{DR} distributions is negatively correlated with RH at all levels and the standard deviation of Z_{DR} is negatively (positively) correlated with RH at all levels below (above) the freezing level. Interestingly, downdraft CAPE (DCAPE) shows the opposite trends and precipitable water (PW/PWAT) shows the same trends as RH. This makes physical sense as PW increases with a larger integrated water vapor mixing ratio in the atmospheric column, while RH also increases with a larger water vapor mixing ratio. DCAPE typically

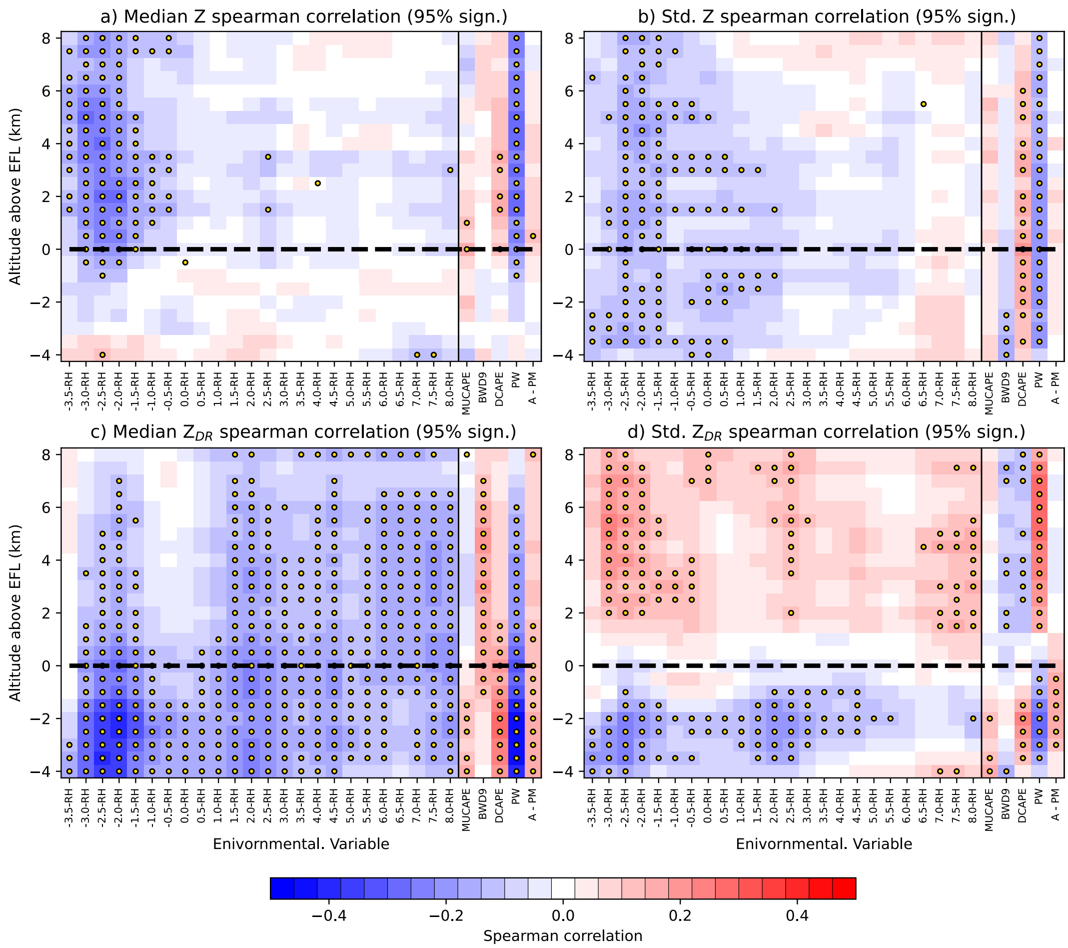

FIG. 5. Spearman's correlation values for every ERA5 meteorological variable and radar distribution (left) median and (right) standard deviation. Stippling indicates the 95% confidence level using the t statistic. The x axes are labeled with meteorological and aerosol variables, and the y axes indicate altitude relative to the freezing level.

decreases with a larger water vapor mixing ratio in a column as it can be described as inversely proportional to the minimum equivalent potential temperature in the lowest 400 hPa of a sounding. The patterns observed with these three variables highlight the effects of a moist (i.e., high RH, high PW, and low DCAPE) and dry tropospheric column on the characteristics of the CFADs. A moist atmospheric column leads to generally smaller Z_H and Z_{DR} magnitudes on average in addition to narrower distributions of these variables except for Z_{DR} above the freezing level, where the distribution is likely wider. While not a goal of this study, it is speculated that these patterns are related to the entrainment of outside air throughout the updraft's vertical extent. If the air is drier, more evaporation can occur with the smallest liquid drops evaporating first, increasing Z_{DR} below the freezing level. The Z_H distributions are likely narrower and somewhat smaller below the freezing level in moist tropospheric conditions as warm rain processes may be more prevalent due to wider DSDs from the presence of smaller drops (Dolan et al. 2018). Thus, cold-phase processes such as riming and freezing may not occur as much at and above the freezing level due to the condensate mass precipitating out in the warm phase, decreasing median Z_H values above the freezing level. The Z_H and Z_{DR} distributions above the freezing level may also be affected by differing ice crystal habits, where larger supersaturations with respect to ice (due to larger RH) promote more assemblages of plates and dendrites (Bailey and Hallett 2009). These particles are more likely to aggregate together, reducing Z_{DR} compared to the drier troposphere cases where plates may not aggregate together as easily and have larger densities.

MUCAPE generally lacks significant correlation with the radar variable distribution characteristics, except below the freezing level where it is positively correlated with the median and standard deviation of Z_{DR}. Physically, this positive correlation may be caused by larger drops produced from updrafts that in theory should have larger vertical velocities due to the increased buoyancy (i.e., MUCAPE). The spectrum of drop sizes produced may also in fact be larger given that the Z_{DR} distribution is typically wider in high MUCAPE environments. Different drop sizes may come from a variety of processes, such as larger amounts of mixed-phase/cold-phase precipitation production and subsequent melting of hail/

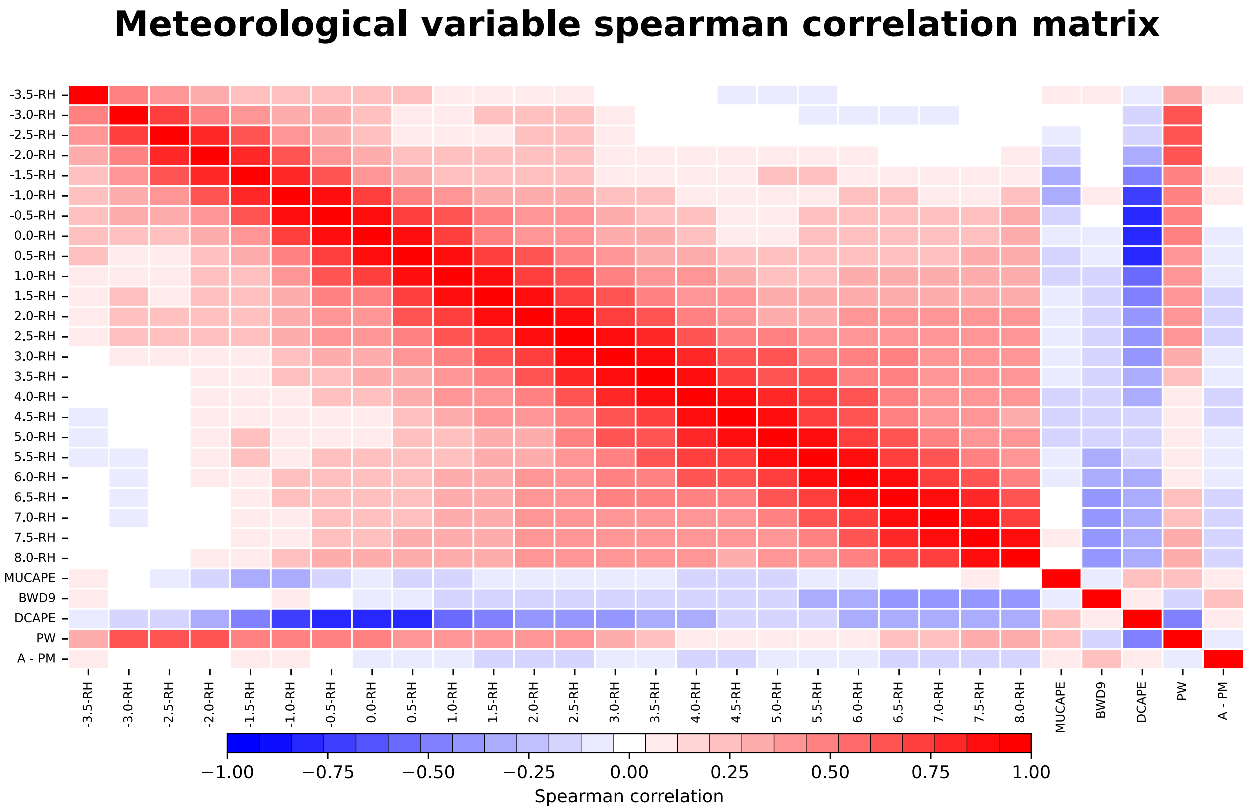

FIG. 6. Spearman's correlation matrix for the meteorological and aerosol variables shown in Fig. 5.

graupel as well as size sorting effects from stronger vertical velocities.

Bulk wind difference in the 0–9-km layer (BWD09) also lacks large areas of strong statistical significance but is weakly correlated with Z_{DR} distribution characteristics near and above the freezing level. There is a positive correlation with the median in Z_{DR} and a negative correlation with the standard deviation in Z_{DR}. With this dataset, it is nearly impossible to attribute the microphysical/dynamical processes that would lead to this correlation. Nevertheless, this analysis aids in the ability to account for meteorological influences on the radar variable distribution characteristics that will be used to assess aerosol effects.

Figure 6 shows the Spearman correlation matrix for all meteorological variables discussed above in addition to A PM$_{2.5}$. The matrix shows the obvious strong positive correlation within RH at neighboring altitudes. Additionally, it shows the strong correlation of PW, DCAPE, and RH with each other which was discussed previously. Most importantly, it illustrates that the maximum Spearman correlation magnitude with A PM$_{2.5}$ is $0.2 \leq r \leq 0.23$, which is with RH in the 6.5–8-km layer above the freezing level. This is important because within the encompassing DCC dataset over land a majority of the meteorological variables do not correlate strongly with the aerosol proxy. However, it is important to note that aerosol–meteorology correlations can still exist within the defined meteorological bins and these correlations are assessed for every subset. Those that exhibit an $r > |0.25|$ are considered as too high of a correlation and are shown in appendix A.

b. *CFADs and microphysical fingerprints*

1) TROPOSPHERIC HUMIDITY

First, differences observed in the high and low A PM$_{2.5}$ regimes under dry and moist tropospheric conditions are presented using the CFADs and MPS plots. The meteorological variable that produced the lowest correlation with A PM$_{2.5}$ within the high and low subsets was DCAPE and is discussed below to illustrate aerosol effects under different tropospheric humidity conditions. The other tropospheric measures of humidity, RH and PW, show very similar signatures (Figs. A2 and A4 in appendix A) but show slightly higher correlations between A PM$_{2.5}$ and the meteorological variable.

Figure 7 shows the composite difference CFADs of Z_H and Z_{DR} and MPS plots for the high DCAPE subset. Below the freezing level, a narrower Z_H distribution that peaks around 20–30 dBZ (Fig. 7a) coupled with slightly larger Z_{DR} dominance > 2 dB (Fig. 7b) for the high A PM$_{2.5}$ DCCs (red pixels) is observed. This signature likely represents an increased probability of more inefficient liquid precipitation because of the more probable 20–30-dBZ range and large Z_{DR}. This is in contrast to the blue pixel regions in Figs. 7a and 7b, where low A PM$_{2.5}$ DCCs are more likely to exhibit Z_{DR} near 0 dB

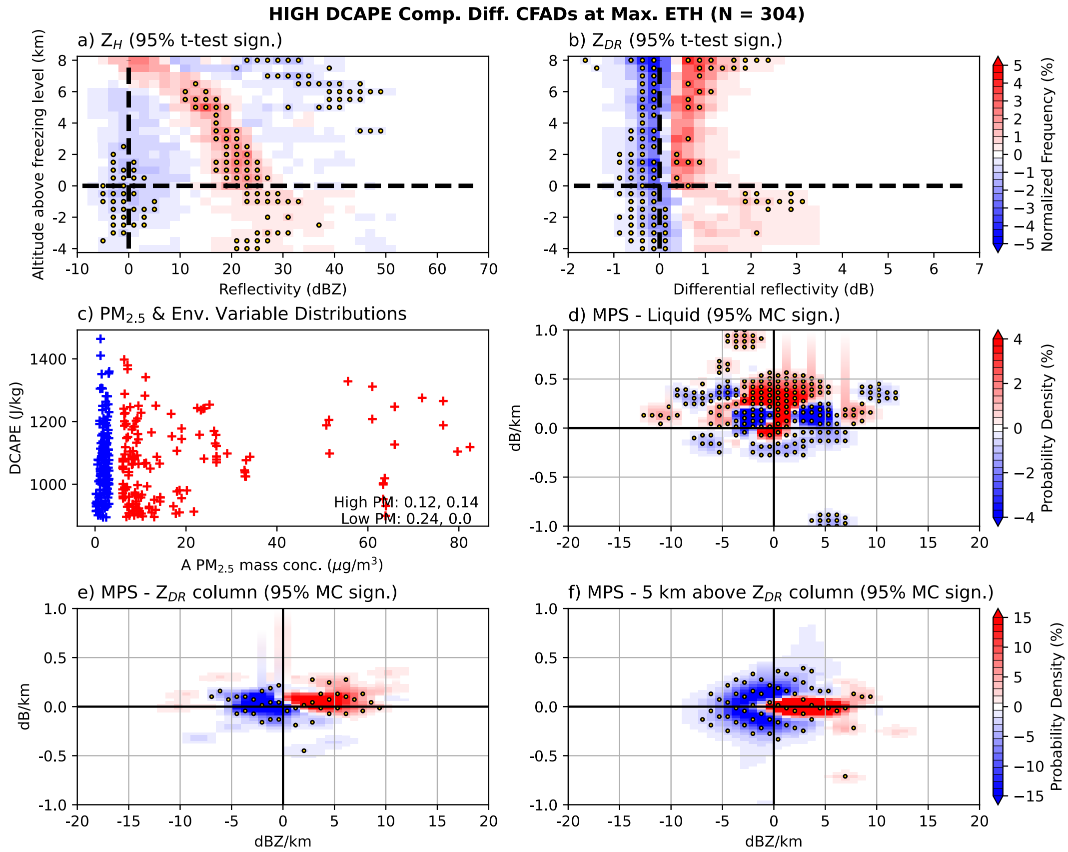

FIG. 7. (a) Composite difference Z_H CFAD, (b) composite difference $Z_{\rm DR}$ CFAD, (c) distribution of A $PM_{2.5}$ mass concentration and DCAPE for all DCCs used in the CFAD calculation, and (d)–(f) composite difference KDEs of the MPS given by ΔZ and $\Delta Z_{\rm DR}$ derived from the CFADs of the DCCs in this subset. For (c), the first number is the Spearman correlation coefficient and the associated two-sided p value. The color bar in the first row corresponds to both CFADs. The color bar in the bottom row corresponds to (e) and (f). Positive (red) values correspond to a higher probability for high A $PM_{2.5}$ DCCs. All DCCs are analyzed at the time of their maximum ETH. Stippling shows 95% significance using a t test for (a) and (b) and using a 5000-iteration Monte Carlo simulation for (d)−(f).

but similar to Z_H in the >30-dBZ range. Concentrations of liquid drops are thus assumed to be higher in the low A $PM_{2.5}$ DCCs in order to produce similar Z_H values above 30 dBZ, given the dependence of Z_H to D^6. Dry tropospheric environments leading to high DCAPE values may increase evaporation rates, especially if numerous small drops are initially formed through the activation of many CCNs in high A $PM_{2.5}$ conditions. Once entrainment of dry air occurs in the updraft, these numerous small drops will quickly evaporate, reducing accretion rates and subsequent precipitation enhancement in the liquid phase. The MPS plot for the liquid region in Fig. 7d somewhat corroborates this theory, where about half the probability of the low A $PM_{2.5}$ DCCs is in the coalescence quadrant (upper right) or balance quadrant (lower right), meaning more liquid precipitation processes. Relative maxima of low A $PM_{2.5}$ DCCs in the evaporation area (upper-left quadrant, close to the x axis) exist, meaning that some of the low A $PM_{2.5}$ DCCs in the dry environments can be susceptible to evaporation effects, just as the high A $PM_{2.5}$ DCCs.

Above the freezing level, high A $PM_{2.5}$ DCCs still exhibit a narrower Z_H distribution in the 10–25-dBZ range coupled with higher probabilities of larger $Z_{\rm DR}$ (0.25 dB). Within the $Z_{\rm DR}$ column region, melting/freezing is much more prevalent in the high A $PM_{2.5}$ DCCs as the red pixels are located almost completely in the melting/freezing quadrant (upper right) in Fig. 7e. Blue pixels are distributed mostly in the negative ΔZ area of the MPS, meaning the low A $PM_{2.5}$ DCCs are more likely to exhibit sublimation or balance between sublimation and melting/freezing processes. Above the $Z_{\rm DR}$ column, Fig. 7f illustrates that vapor deposition is much more likely in the high A $PM_{2.5}$ DCCs, whereas all other cold-phase processes such as freezing, sublimation, and aggregation are more likely for low A $PM_{2.5}$ DCCs. Other than certain types of freezing processes, these cold-phase processes lead to a decrease in $Z_{\rm DR}$, while Z_H can be affected more by the concentration of subsequent frozen particles (i.e., rates of these processes). Since the CFADs in Fig. 7 show similar probabilities that Z_H > 25 dBZ but $Z_{\rm DR} \le 0$ dB is more likely for low A $PM_{2.5}$ DCCs, it can be assumed that these DCCs exhibit

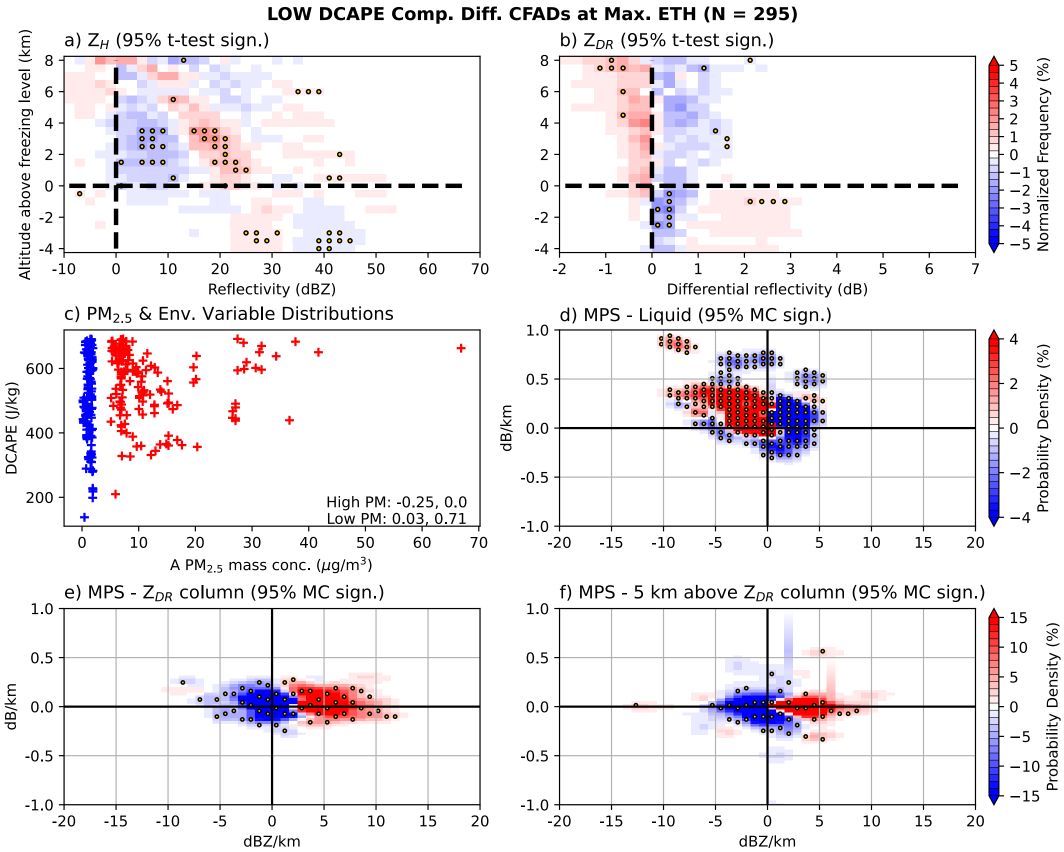

FIG. 8. As in Fig. 7, but for DCCs within the LOW DCAPE tercile.

greater rates of these cold-phase precipitation processes in dry tropospheric environments.

DCCs within the low DCAPE subset exhibit different patterns than those observed in the high DCAPE regime when comparing across high and low A $PM_{2.5}$. Figure 8 generally illustrates that the differences observed in the composite difference CFADs are smaller in magnitude and lack larger areas of significance compared to the high DCAPE regime and are consistent throughout the other measures of tropospheric humidity (Figs. A1 and A3). Each moist tropospheric measure still exhibits a narrower Z_H distribution for high A $PM_{2.5}$ DCCs below and above the freezing level, but the differences are less pronounced compared to the dry counterparts. In general, high A $PM_{2.5}$ DCCs are more likely to be in the size sorting/evaporation quadrant of the MPS plot, while the low A $PM_{2.5}$ DCCs are more likely to be in the coalescence or balance quadrants (Fig. 8d), which is expected for conditions of high aerosol loading and points to a diminishing of the warm rain process. However, the typical notion that this delay in the warm rain process under humid conditions leads to more efficient riming and accretion processes does not appear to be supported, as Z_{DR} is more likely to be $\geq$0.25 dB above the freezing level for low A $PM_{2.5}$ DCCs. This is also corroborated by Fig. 8e where very little of the red pixels are in the aggregation/riming quadrant and are more skewed toward the melting/freezing quadrant. Given that Z_H is likely to be the same in the Z_{DR} column altitudes (i.e., $0 \leq z \leq 2$ km) for $Z_H > 30$ dBZ, it can be assumed that the high A $PM_{2.5}$ DCCs have larger concentrations of particles which is consistent with increased transport of liquid drops to the freezing level from the inhibition of warm rain, leading to larger freezing rates and thus lower Z_{DR}. This mechanism could be a reason that riming and accretion could possibly be larger in the high A $PM_{2.5}$ DCCs as discussed earlier, but the freezing rates may also be enhanced and mask the polarimetric retrievals. Nevertheless, even with these possible microphysical changes, precipitation efficiency seems to be diminished as the largest Z_H values below the freezing level are more likely to be from the low A $PM_{2.5}$ DCCs in moist tropospheric conditions.

2) INSTABILITY

Figure 9 generally shows that environments with large instability promote similar differences in the statistical distributions of radar data as those found in dry tropospheric conditions (i.e., Fig. 7). In fact, the CFADs exhibit even larger Z_H and Z_{DR} distribution differences with wide areas of significance both above and below the freezing level in the Z_{DR} CFAD. This suggests that even with large instability, riming and accretion processes from the inhibition of warm rain in high A $PM_{2.5}$ DCCs may not be largely more efficient than in low A $PM_{2.5}$ DCCs. Instead, it appears that the proposed

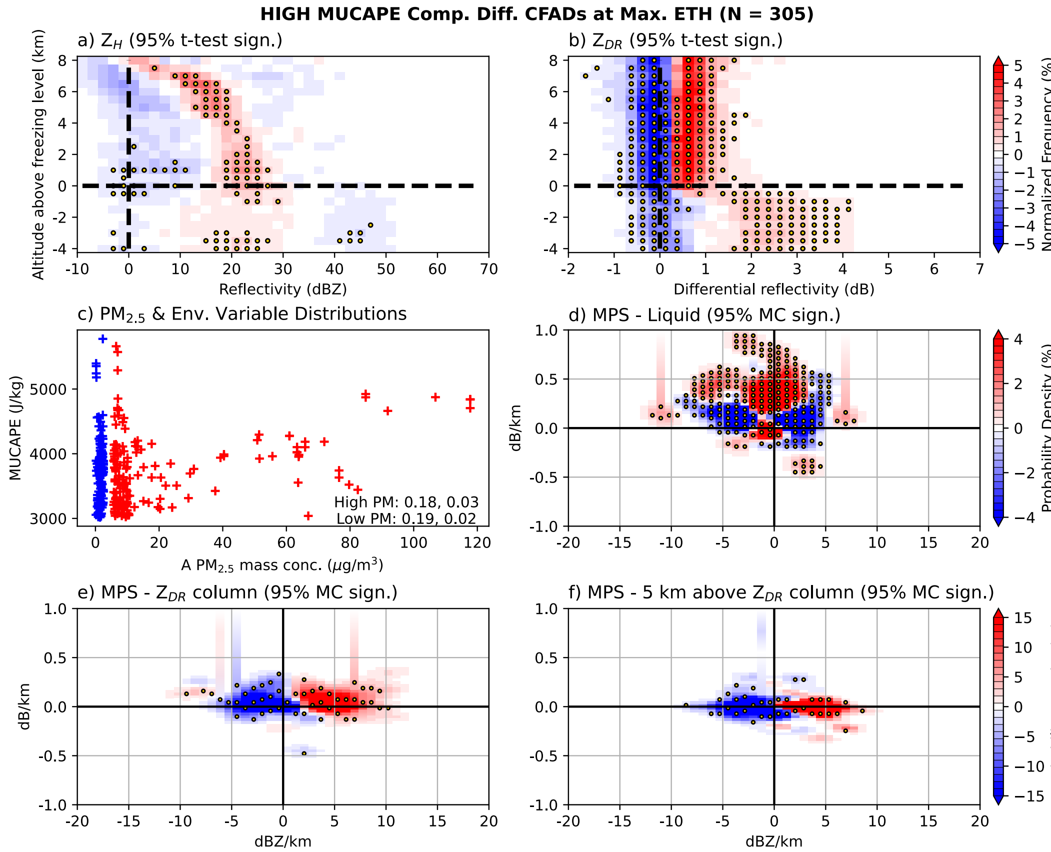

FIG. 9. As in Fig. 7, but for DCCs within the HIGH MUCAPE tercile.

mechanism of increased transport of supercooled droplets to the freezing level increases melting and freezing signatures more so than riming/accretion (Fig. 9e). Moreover, precipitation enhancement does not seem to occur with increased aerosol loading due to $Z_H > 35$ dBZ being slightly dominated by low A $PM_{2.5}$ DCCs. Finally, the consistent signature seen in all other subsets of increased probability of vapor deposition is present again in the above-Z_{DR} column MPS plot (Fig. 9f).

Low instability environments generally exhibit similar differences to those observed for the moist tropospheric conditions (Fig. 10). These results again point to an increased probability of warm rain delay under high aerosol loading since a majority of the red pixels are in the size sorting/evaporation quadrant in Fig. 10d. Riming/accretion rates in the mixed-phase region are still low since Z_{DR} is likely to be smaller for high A $PM_{2.5}$ DCCs in Z_{DR} column region, albeit the differences are not statistically significant (Fig. 10b).

3) WIND SHEAR

The differences observed between high and low A $PM_{2.5}$ DCCs in high-shear environments are presented in Fig. 11. Differences in the Z_H distributions at all altitudes lack coherent patterns of statistical significance (Fig. 11a), but the Z_{DR} distribution differences are quite pronounced (Fig. 11b). Given that Z_H is similar and Z_{DR} is likely to be larger at all altitudes for high A $PM_{2.5}$ DCCs, particle concentration is likely to be smaller for high A $PM_{2.5}$ DCCs throughout the vertical extent. This would indicate that increased shear leads to hindrances in precipitation rates for high A $PM_{2.5}$ DCCs as smaller particles are more easily carried away or evaporate/sublimate from increased entrainment. The MPS plots in Figs. 11d–f all show similar differences in microphysical fingerprints between high and low A $PM_{2.5}$ DCCs as the subsets discussed in the previous two subsections. Namely, that higher aerosol loading leads to decreased warm rain processes, increased freezing/melting, and increased vapor deposition.

Low-shear environments also promote similar differences to those found in the moist tropospheric and low instability conditions (Fig. 12). These differences include lack of dominance of higher Z_{DR} coupled with a narrower Z_H distribution above the freezing level by the high A $PM_{2.5}$ and little to no differences in Z_H below the freezing level. Collectively, these differences support aerosol loading hindrance to precipitation enhancement but observable microphysical changes both above and below the freezing level outlined in the MPS plots (Figs. 12d–f).

4. Conclusions

This study constructed a bulk statistical framework using dual-polarization radar data from KHGX, model reanalysis

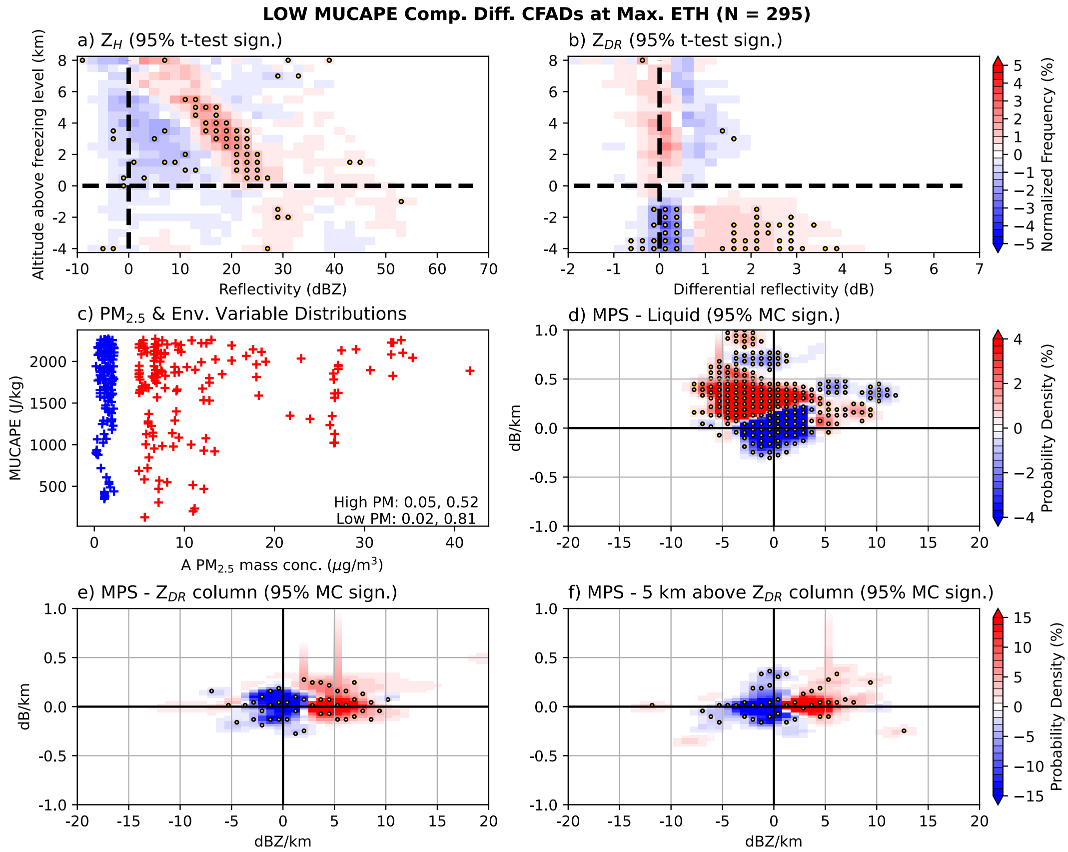

FIG. 10. As in Fig. 7, but for DCCs within the LOW MUCAPE tercile.

data from the ERA5, and aerosol data from the MERRA-2 to examine the effects of aerosol loading on DCCs within the Houston area for the time period 2013–21. Composite difference CFADs of Z_H and Z_{DR} were used to describe mean differences in the vertical radar profiles of DCCs under differing aerosol loadings while constraining DCCs to similar meteorological conditions that are described by previous work. Within this analysis, it was found that statistically significant differences in the distributions of dual-polarization operational S-band radar data and resulting microphysical fingerprints can be identified with a large sample size.

Observed differences in the radar data distributions within this study are generally consistent with previously established theories regarding aerosol effects on deep convection; however, there are some differences. A bulleted summary of these is provided below, with effect categories assigned based on Fig. 11 from Cheng et al. (2010) which describes the major effects of increased CCN on warm- and cold-phase precipitation production.

1) Higher aerosol loading appears to have a negative impact on the collision coalescence process in the liquid phase. This is because many of the MPS plots in the liquid phase (panel d in Figs. 7–A4) show that DCCs under higher aerosol loading are more likely to have reduced collision–coalescence signatures (effect A). This is in agreement with the conclusions reached by Hu et al. (2019a) and Marinescu et al. (2021).
2) Elevated evaporation rates that are typically associated with increased aerosol loading are more difficult to precisely identify but are more probable in high tropospheric moisture regimes (panel d in Figs. 8, A1, and A3) (effect A). The physical explanation for this is difficult to ascertain for an observational study such as this but could be related to less evaporation of low A $PM_{2.5}$ DCCs' early onset of precipitation in moist cases, causing the high A $PM_{2.5}$ DCCs to exhibit higher evaporation rates at this stage of their life cycle. This is consistent with findings by Tao et al. (2007).
3) Riming/accretion can be enhanced in the mixed-phase region depending on meteorological conditions. This was found through analysis of CFADs and Z_{DR} column MPS plots in Figs. 9 and 11. These differences suggest that drier tropospheric conditions, larger instability, and higher shear magnitudes may favor this microphysical response to higher aerosol loading (effect C). The larger instability cases are consistent with Hu et al. (2019a) and Fan et al. (2009), but the drier and larger shear cases are not, which could be due to potential uncertainties in Z_{DR} retrievals in mixed-phase regions. Riming/accretion appears to be inhibited in the other extremes of these meteorological environments, such as moist tropospheric conditions, weaker

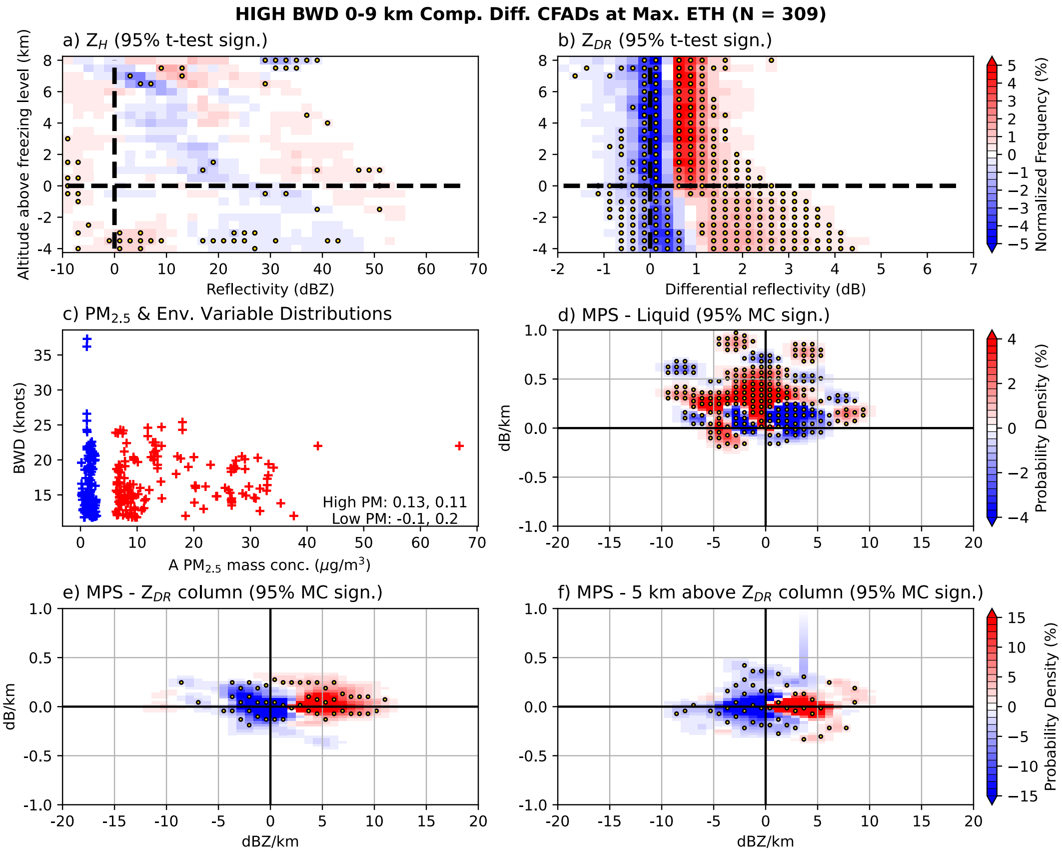

FIG. 11. As in Fig. 7, but for DCCs within the HIGH BWD09 tercile.

instability, and lower shear magnitudes (Figs. 8, 10, and 12) (effect B).

4) Freezing is enhanced regardless of meteorological conditions since all MPS plots within the Z_{DR} column region and above show higher probabilities of red pixels in the freezing quadrant (panels e and f in Figs. 7–A4) (effect D). This is consistent with conclusions presented by Marinescu et al. (2021).
5) Vapor deposition appears to be heavily promoted regardless of meteorological influence, as all MPS plots in the region above the Z_{DR} column show large probabilities for the DCCs under high aerosol loading (panel f in Figs. 7–A4) (effect D). This is consistent with conclusions presented by Marinescu et al. (2021).

The differences and conclusions reached for DCC subsets presented in section 3 are only valid in a mean sense when comparing numerous DCCs under similar (but not the same) meteorological environments. It is possible that the differences observed here are driven by environmental/meteorological differences that are not captured in this bulk analysis. This means that while statistically significant differences in polarimetric radar data were found when using a large sample size in this experiment, aerosols are not the only variable affecting microphysical processes within DCCs. Further, only differences in cloud properties, and not processes, can be obtained from observations such as those within this study. Modeling studies that turn on and off various aerosol processes are needed to understand the reasons for the observed differences. Additionally, there are limitations for uncovering aerosol effects on DCCs in this study that lead to some uncertainties, namely, the coarse resolution of data, parameterizations of MERRA-2's $PM_{2.5}$ mass concentration as a proxy for CCN number concentration, ERA5's inability to resolve interactions of DCCs with one another and sea-breeze boundaries, the dependency of the results on the sensitivity of MCIT, and uncertainties involving polarimetric retrievals. To mitigate these uncertainties, future work should compare the use of a Z_{DR} column algorithm with the current ETH method to gain further insights into how aerosol loading changes the temporal evolution of Z_{DR} column heights in DCCs. The problem of the coarse resolution of the meteorological and aerosol data could be improved by including additional data, such as those of the North American Regional Reanalysis or High-Resolution Rapid Refresh reanalysis, which have data available similar to ERA5 to compare results, and the inclusion of a second aerosol dataset consisting of satellite-retrieved CCN number concentration estimates (e.g., Hu et al. 2019a). These estimates would also greatly improve the uncertainty caused by the parameterizations of

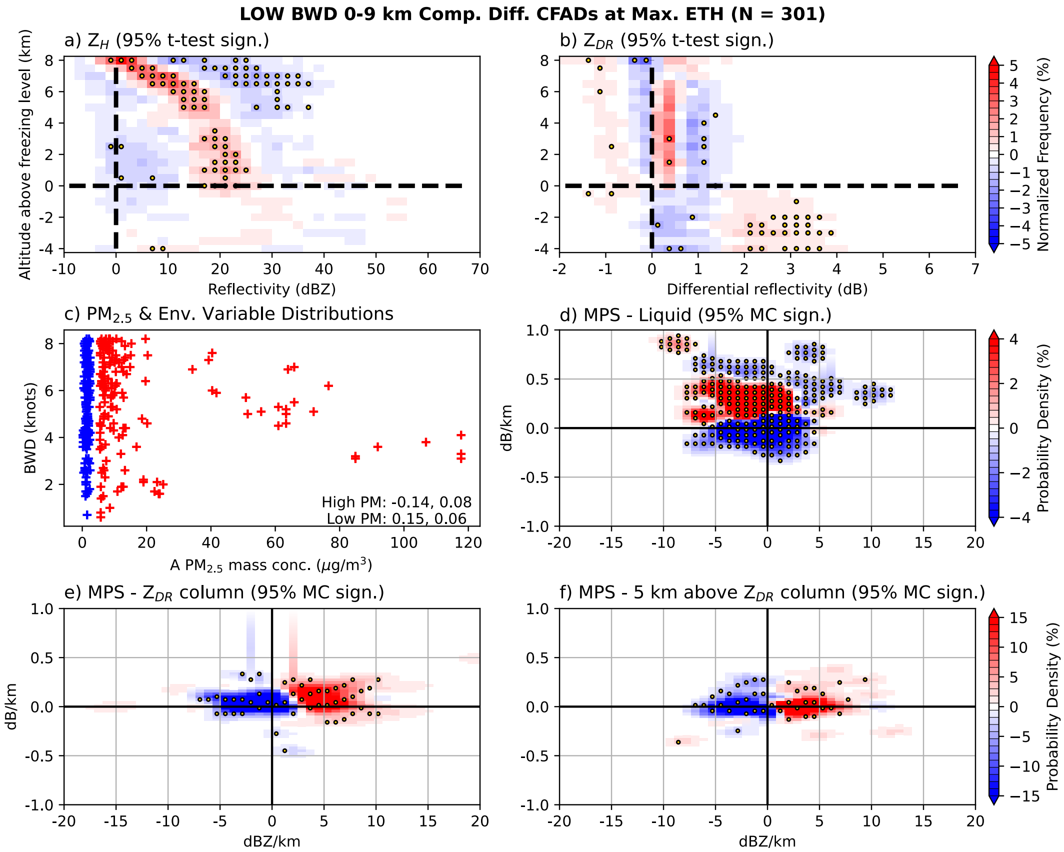

FIG. 12. As in Fig. 7, but for DCCs within the LOW BWD09 tercile.

MERRA-2's $PM_{2.5}$ representation. With the two aerosol datasets, much work could be done in validating MERRA-2's ability to estimate periods of high CCN loading and compare the results of this study when using satellite-retrieved estimates. Also, the dependency of the results on the MCIT algorithm parameters could be quantified by using sensitivity tests that change the MCIT thresholds such as minimum valley depth, minimum cell size, and minimum cell depth which would allow for easier temporal analysis of DCC evolution in regards to aerosol effects. Finally, comparisons with in situ field campaigns such as the Experiment of Sea Breeze Convection, Aerosols, Precipitation, and Environment (ESCAPE) should also be done to establish potential biases in gridded and remote sensing aerosol, cloud, and atmospheric state datasets. This would aid in alleviating uncertainties regarding actual DCC CCN ingestion and how reliable $PM_{2.5}$ is for assessing CCN size distributions at a cloud base.

Acknowledgments. We acknowledge support from the National Science Foundation Atmospheric and Geospace Science under Grant NSF AGS-2019968. We would also like to acknowledge Jiaxi Hu from CIWRO, Horst Severini and Brad Spitzbart from the University of Oklahoma's Supercomputing Center for Education and Research (OSCER), and John Krause from NSSL for help in generating preliminary research ideas and aid in using the Schooner supercomputer and MCIT. The computing for this project was performed at the OSCER at the University of Oklahoma (OU). Finally, acknowledgment is extended to Vitor Goede for aid in code needed to generate ERA5 soundings.

Data availability statement. The ERA5 data can be accessed at https://cds.climate.copernicus.eu. The MERRA-2 data can be accessed at https://disc.gsfc.nasa.gov/datasets. MCIT data used in this study are available upon request to the first author by emailing jonah.pehl@ou.edu.

APPENDIX A

Additional Tropospheric Humidity Subsets

Figures A1–A4 show the composite difference CFADs and MPS plots for DCCs binned by tropospheric humidity measures, specifically median column RH and PWAT. As a reminder, Figs. A1 and A3 represent moist conditions (high RH and PWAT), while Figs. A2 and A4 represent dry conditions (low RH and PWAT). The CFADs and MPS plots in each of the figures show similar patterns to their DCAPE counterparts discussed in section 3b(1).

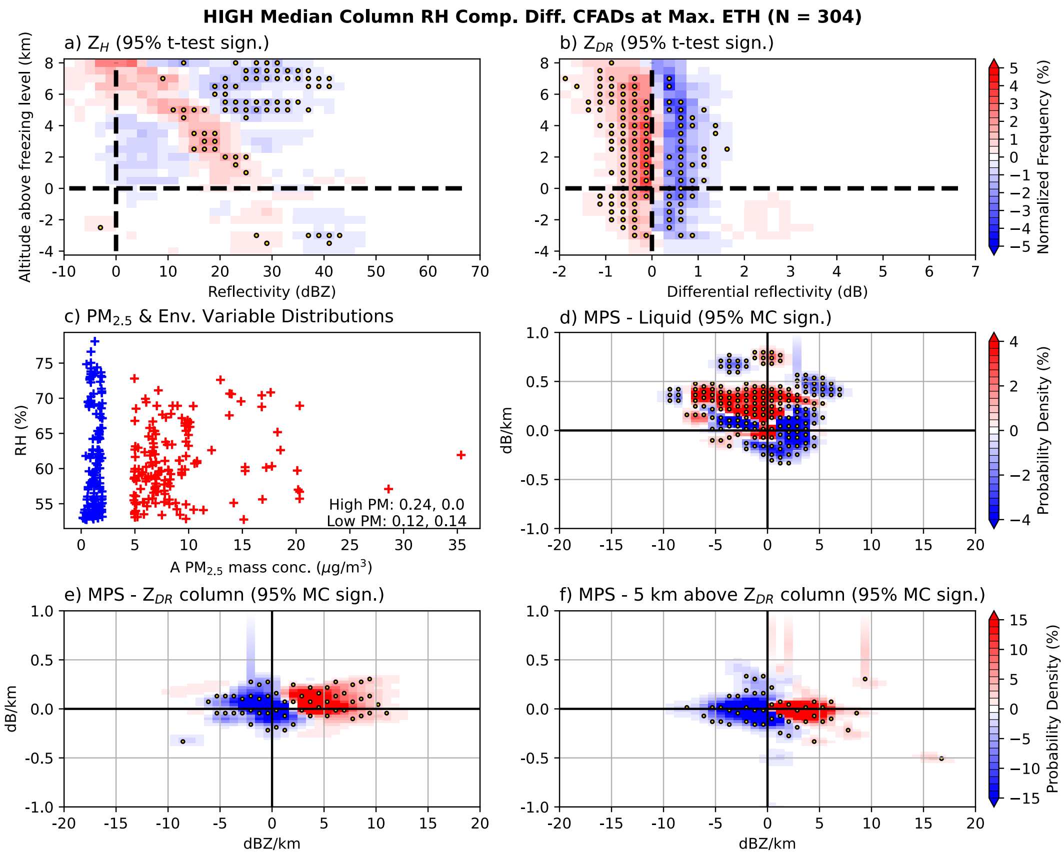

FIG. A1. As in Fig. 7, but for DCCs within the HIGH RH tercile.

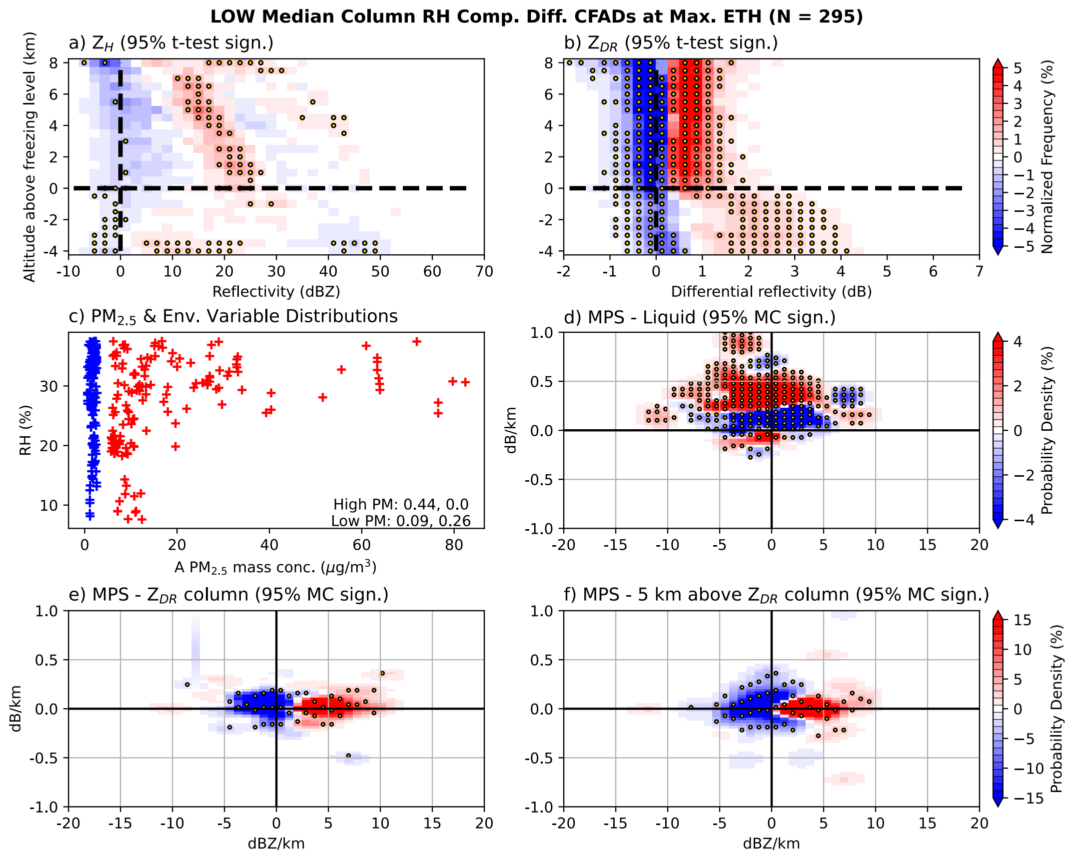

FIG. A2. As in Fig. 7, but for DCCs within the LOW RH tercile.

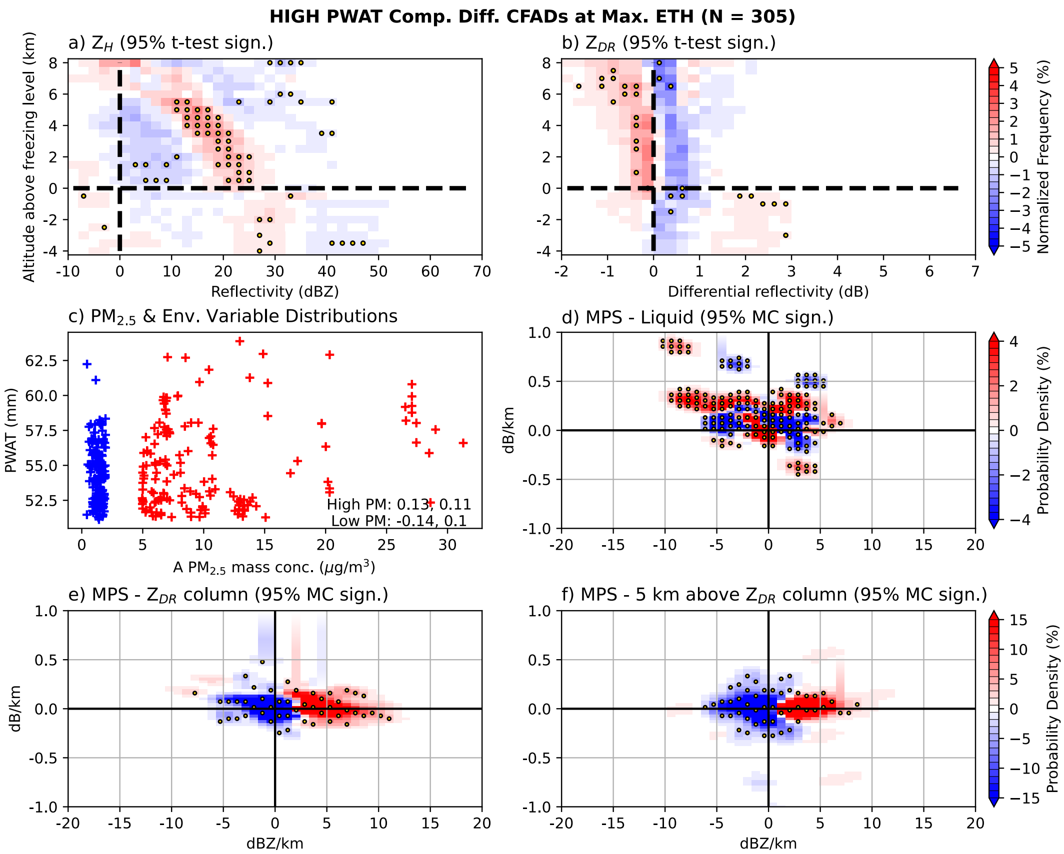

FIG. A3. As in Fig. 7, but for DCCs within the HIGH PW tercile.

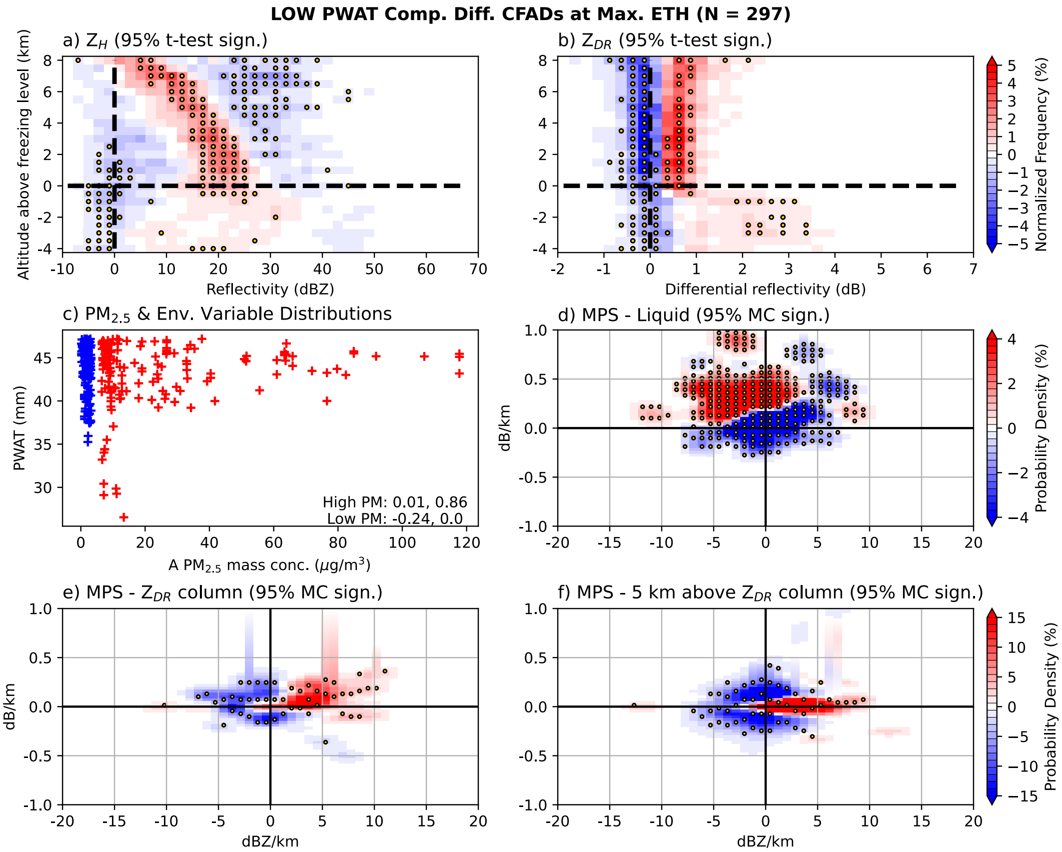

FIG. A4. As in Fig. 7, but for DCCs within the LOW PW tercile.

APPENDIX B

Additional Statistical Dataset Properties

Figures B1–B3 are provided below to present additional information about the properties of the DCCs used in the statistical analysis. Table B1 defines important acronyms and definitions used in the study.

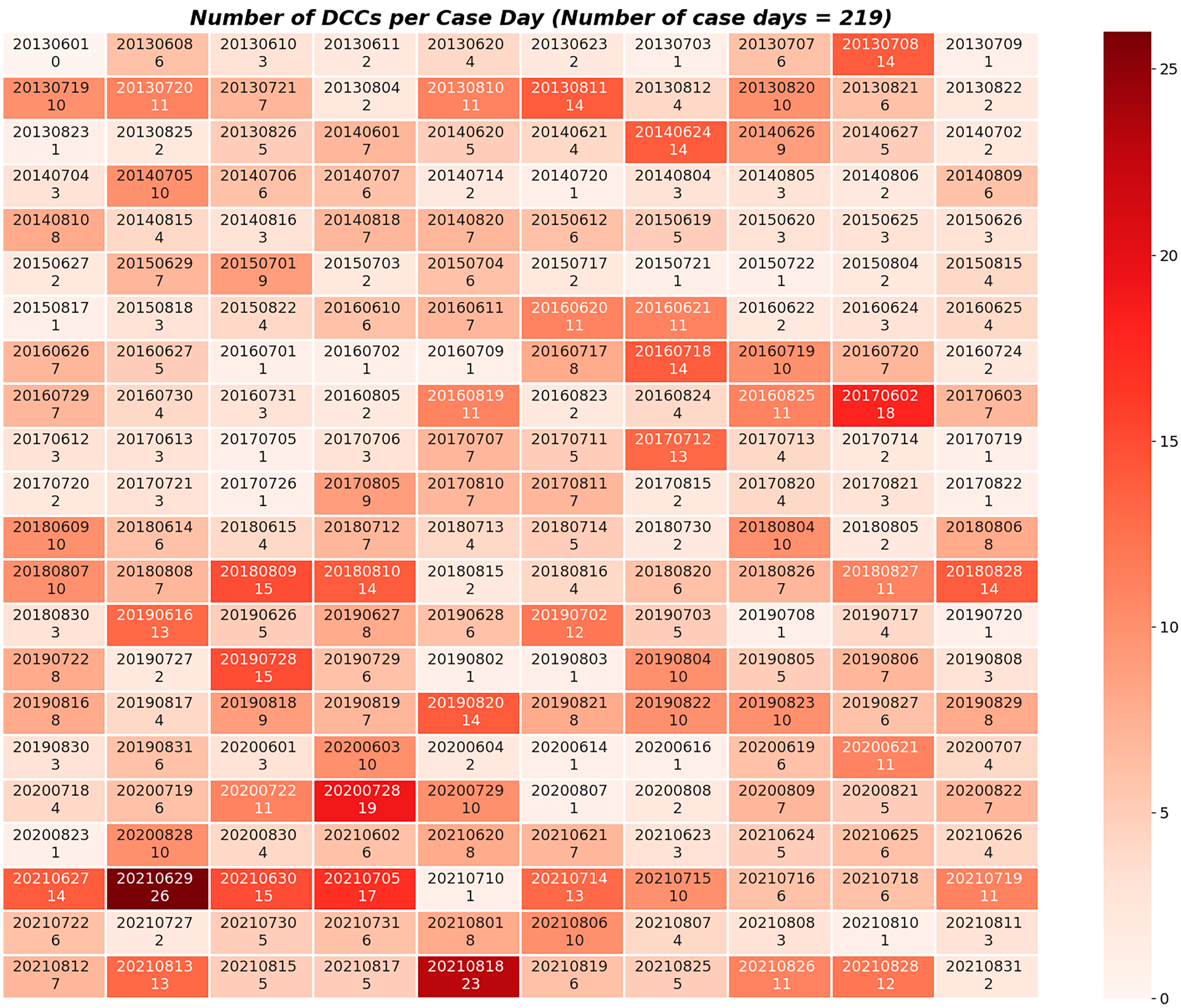

FIG. B1. Number of DCCs per case day used in the study.

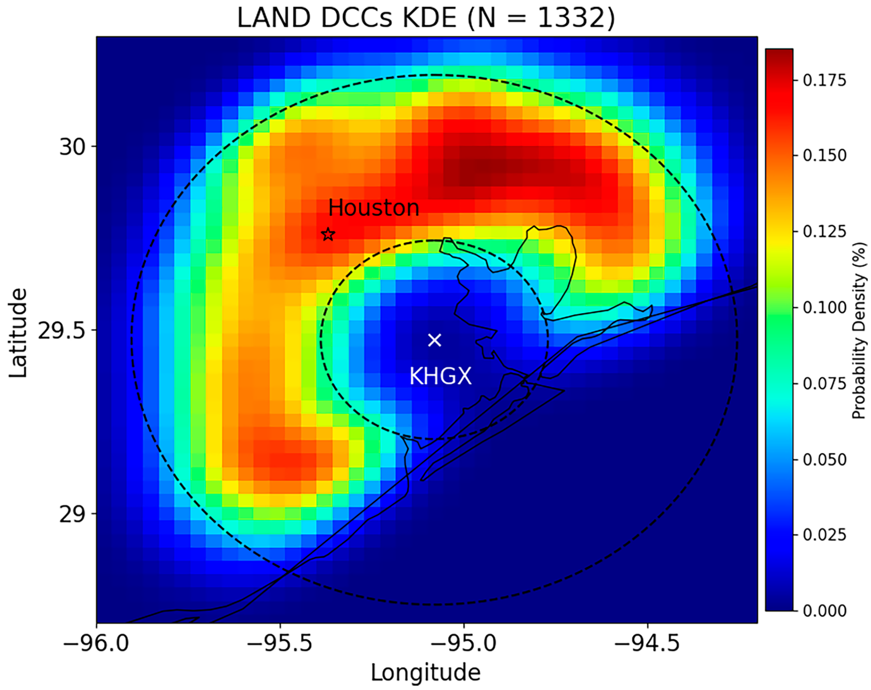

FIG. B2. KDE of all LAND DCCs' locations of maximum ETH used in this study.

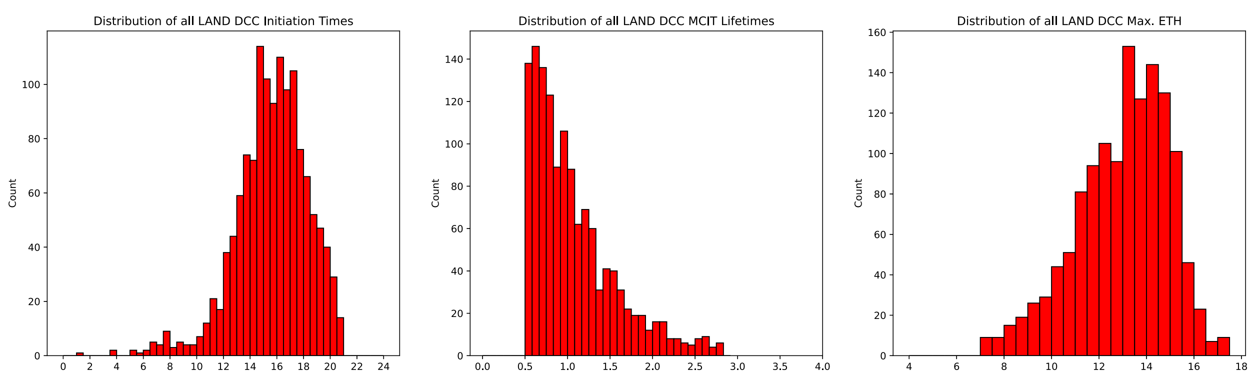

FIG. B3. Distributions of (left) DCC initiation times relative to 1200 central daylight time (CDT), (center) lifetimes in the MCIT algorithm, and (right) maximum ETH achieved.

TABLE B1. Important acronym definitions.

Acronym	Phrase
A	Anthropogenic
BWD09	Bulk wind difference in the 0–9-km layer
CCN	Cloud condensation nuclei
CFAD	Contoured frequency by altitude diagram
DCC	Deep convective cloud
DSD	Drop size distribution
EFL	Environmental freezing level
ERA5	Fifth major global reanalysis produced by ECMWF
ETH	Echo top height
MAIE	Mixed-phase aerosol invigoration effect
MCIT	Multi-Cell and Identification Tracking
MERRA-2	Modern-Era Retrospective Analysis for Research and Applications, version 2
MPS	Microphysical parameter space
MUCAPE	Most unstable convective available potential energy
$PM_{2.5}$	Particulate matter (diameter $\leq 2.5\ \mu$m)
PW/PWAT	Precipitable water
QVP	Quasi-vertical profile
RH	Median column RH (-3.5 to 8 km above freezing level)
z	Height coordinate relative to freezing level (km)

REFERENCES

Albrecht, B. A., 1989: Aerosols, cloud microphysics, and fractional cloudiness. *Science*, **245**, 1227–1230, https://doi.org/10.1126/science.245.4923.1227.

Altaratz, O., I. Koren, L. A. Remer, and E. Hirsch, 2014: Review: Cloud invigoration by aerosols—Coupling between microphysics and dynamics. *Atmos. Res.*, **140–141**, 38–60, https://doi.org/10.1016/j.atmosres.2014.01.009.

Andreae, M. O., D. Rosenfeld, P. Artaxo, A. A. Costa, G. P. Frank, K. M. Longo, and M. A. F. Silva-Dias, 2004: Smoking rain clouds over the Amazon. *Science*, **303**, 1337–1342, https://doi.org/10.1126/science.1092779.

Bailey, M. P., and J. Hallett, 2009: A comprehensive habit diagram for atmospheric ice crystals: Confirmation from the laboratory, AIRS II, and other field studies. *J. Atmos. Sci.*, **66**, 2888–2899, https://doi.org/10.1175/2009JAS2883.1.

Bell, T. L., D. Rosenfeld, K.-M. Kim, J.-M. Yoo, M.-I. Lee, and M. Hahnenberger, 2008: Midweek increase in U.S. summer rain and storm heights suggests air pollution invigorates rainstorms. *J. Geophys. Res.*, **113**, D02209, https://doi.org/10.1029/2007JD008623.

Bluestein, H. B., D. T. Lindsey, D. Bikos, D. W. Reif, and Z. B. Wienhoff, 2019: The relationship between overshooting tops in a tornadic supercell and its radar-observed evolution. *Mon. Wea. Rev.*, **147**, 4151–4176, https://doi.org/10.1175/MWR-D-19-0159.1.

Boucher, O., and J. Quaas, 2013: Water vapour affects both rain and aerosol optical depth. *Nat. Geosci.*, **6**, 4–5, https://doi.org/10.1038/ngeo1692.

Carrió, G. G., W. R. Cotton, and W. Y. Y. Cheng, 2010: Urban growth and aerosol effects on convection over Houston: Part I: The August 2000 case. *Atmos. Res.*, **96**, 560–574, https://doi.org/10.1016/j.atmosres.2010.01.005.

Chen, T., Z. Li, R. A. Kahn, C. Zhao, D. Rosenfeld, J. Guo, W. Han, and D. Chen, 2021: Potential impact of aerosols on convective clouds revealed by Himawari-8 observations over different terrain types in eastern China. *Atmos. Chem. Phys.*, **21**, 6199–6220, https://doi.org/10.5194/acp-21-6199-2021.

Cheng, C.-T., W.-C. Wang, and J.-P. Chen, 2010: Simulation of the effects of increasing cloud condensation nuclei on mixed-phase clouds and precipitation of a front system. *Atmos. Res.*, **96**, 461–476, https://doi.org/10.1016/j.atmosres.2010.02.005.

Cotton, W. R., and R. Walko, 2021: Examination of aerosol-induced convective invigoration using idealized simulations. *J. Atmos. Sci.*, **78**, 287–298, https://doi.org/10.1175/JAS-D-20-0023.1.

Dagan, G., I. Koren, and O. Altaratz, 2015: Aerosol effects on the timing of warm rain processes. *Geophys. Res. Lett.*, **42**, 4590–4598, https://doi.org/10.1002/2015GL063839.

Dolan, B., B. Fuchs, S. A. Rutledge, E. A. Barnes, and E. J. Thompson, 2018: Primary modes of global drop size distributions. *J. Atmos. Sci.*, **75**, 1453–1476, https://doi.org/10.1175/JAS-D-17-0242.1.

Donaldson, R. J., Jr., 1964: A demonstration of antenna beam errors in radar reflectivity patterns. *J. Appl. Meteor.*, **3**, 611–623, https://doi.org/10.1175/1520-0450(1964)003<0611:ADOABE>2.0.CO;2.

Doviak, R. J., D. S. Zrnic, and R. M. Schotland, 1994: Doppler radar and weather observations. *Appl. Opt.*, **33**, 4531.

Duan, J., and Coauthors, 2018: Influence of pollutants on activity of aerosol cloud condensation nuclei (CCN) during pollution and post-rain periods in Guangzhou, southern China. *Sci. Total Environ.*, **642**, 1008–1019, https://doi.org/10.1016/j.scitotenv.2018.06.053.

Dworak, R., K. Bedka, J. Brunner, and W. Feltz, 2012: Comparison between *GOES-12* overshooting-top detections, WSR-88D radar reflectivity, and severe storm reports. *Wea. Forecasting*, **27**, 684–699, https://doi.org/10.1175/WAF-D-11-00070.1.

Evans, J. E., K. Carusone, M. M. Wolfson, M. Robinson, E. Ducot, and B. Crowe, 2004: Improving convective weather operations in highly congested airspace with the Corridor Integrated Weather System (CIWS). *11th Conf. on Aviation, Range and Aerospace Meteorology*, Hyannis, MA, Amer. Meteor. Soc., P1.5, https://ams.confex.com/ams/11aram22sls/meetingapp.cgi/Paper/81276.

Fan, J., and A. Khain, 2021: Comments on "Do ultrafine cloud condensation nuclei invigorate deep convection?" *J. Atmos. Sci.*, **78**, 329–339, https://doi.org/10.1175/JAS-D-20-0218.1.

——, R. Zhang, G. Li, and W.-K. Tao, 2007: Effects of aerosols and relative humidity on cumulus clouds. *J. Geophys. Res.*, **112**, D14204, https://doi.org/10.1029/2006JD008136.

——, and Coauthors, 2009: Dominant role by vertical wind shear in regulating aerosol effects on deep convective clouds. *J. Geophys. Res.*, **114**, D22206, https://doi.org/10.1029/2009JD012352.

——, D. Rosenfeld, Y. Ding, L. R. Leung, and Z. Li, 2012: Potential aerosol indirect effects on atmospheric circulation and radiative forcing through deep convection. *Geophys. Res. Lett.*, **39**, L09806, https://doi.org/10.1029/2012GL051851.

——, L. R. Leung, D. Rosenfeld, Q. Chen, Z. Li, J. Zhang, and H. Yan, 2013: Microphysical effects determine macrophysical response for aerosol impacts on deep convective clouds. *Proc. Natl. Acad. Sci. USA*, **110**, E4581–E4590, https://doi.org/10.1073/pnas.1316830110.

——, Y. Wang, D. Rosenfeld, and X. Liu, 2016: Review of aerosol–cloud interactions: Mechanisms, significance, and challenges. *J. Atmos. Sci.*, **73**, 4221–4252, https://doi.org/10.1175/JAS-D-16-0037.1.

——, and Coauthors, 2018: Substantial convection and precipitation enhancements by ultrafine aerosol particles. *Science*, **359**, 411–418, https://doi.org/10.1126/science.aan8461.

——, Y. Zhang, Z. Li, J. Hu, and D. Rosenfeld, 2020: Urbanization-induced land and aerosol impacts on sea-breeze circulation and convective precipitation. *Atmos. Chem. Phys.*, **20**, 14 163–14 182, https://doi.org/10.5194/acp-20-14163-2020.

Fuchs, B. R., and Coauthors, 2015: Environmental controls on storm intensity and charge structure in multiple regions of the continental United States. *J. Geophys. Res. Atmos.*, **120**, 6575–6596, https://doi.org/10.1002/2015JD023271.

Givati, A., and D. Rosenfeld, 2004: Quantifying precipitation suppression due to air pollution. *J. Appl. Meteor.*, **43**, 1038–1056, https://doi.org/10.1175/1520-0450(2004)043<1038:QPSDTA>2.0.CO;2.

Grabowski, W. W., 2015: Untangling microphysical impacts on deep convection applying a novel modeling methodology. *J. Atmos. Sci.*, **72**, 2446–2464, https://doi.org/10.1175/JAS-D-14-0307.1.

——, 2018: Can the impact of aerosols on deep convection be isolated from meteorological effects in atmospheric observations? *J. Atmos. Sci.*, **75**, 3347–3363, https://doi.org/10.1175/JAS-D-18-0105.1.

——, and H. Morrison, 2016: Untangling microphysical impacts on deep convection applying a novel modeling methodology. Part II: Double-moment microphysics. *J. Atmos. Sci.*, **73**, 3749–3770, https://doi.org/10.1175/JAS-D-15-0367.1.

——, and ——, 2020: Do ultrafine cloud condensation nuclei invigorate deep convection? *J. Atmos. Sci.*, **77**, 2567–2583, https://doi.org/10.1175/JAS-D-20-0012.1.

Held, G., 1978: The probability of hail in relation to radar echo heights on the South African Highveld. *J. Appl. Meteor.*, **17**, 755–762, https://doi.org/10.1175/1520-0450(1978)017<0755:TPOHIR>2.0.CO;2.

Hersbach, H., and Coauthors, 2020: The ERA5 global reanalysis. *Quart. J. Roy. Meteor. Soc.*, **146**, 1999–2049, https://doi.org/10.1002/qj.3803.

Hu, J., and Coauthors, 2019a: Polarimetric radar convective cell tracking reveals large sensitivity of cloud precipitation and electrification properties to CCN. *J. Geophys. Res. Atmos.*, **124**, 12 194–12 205, https://doi.org/10.1029/2019JD030857.

——, and Coauthors, 2019b: Tracking and characterization of convective cells through their maturation into stratiform storm elements using polarimetric radar and lightning detection. *Atmos. Res.*, **226**, 192–207, https://doi.org/10.1016/j.atmosres.2019.04.015.

Huang, J., Q. Fu, J. Su, Q. Tang, P. Minnis, Y. Hu, Y. Yi, and Q. Zhao, 2009: Taklimakan dust aerosol radiative heating derived from CALIPSO observations using the Fu-Liou radiation model with CERES constraints. *Atmos. Chem. Phys.*, **9**, 4011–4021, https://doi.org/10.5194/acp-9-4011-2009.

Ilotoviz, E., A. Khain, A. V. Ryzhkov, and J. C. Snyder, 2018: Relationship between aerosols, hail microphysics, and z_{DR} columns. *J. Atmos. Sci.*, **75**, 1755–1781, https://doi.org/10.1175/JAS-D-17-0127.1.

IPCC, 2007: *Climatic Change 2007: The Physical Science Basis*. Cambridge University Press, 996 pp.

——, 2023: Summary for policymakers. *Climate Change 2023: Synthesis Report*, H. Lee and J. Romero, Eds., IPCC, 35–115, https://doi.org/10.59327/IPCC/AR6-9789291691647.001.

Jirak, I. L., and W. R. Cotton, 2006: Effect of air pollution on precipitation along the front range of the Rocky Mountains. *J. Appl. Meteor. Climatol.*, **45**, 236–245, https://doi.org/10.1175/JAM2328.1.

Khain, A. P., 2009: Notes on state-of-the-art investigations of aerosol effects on precipitation: A critical review. *Environ. Res. Lett.*, **4**, 015004, https://doi.org/10.1088/1748-9326/4/1/015004.

——, D. Rosenfeld, and A. Pokrovsky, 2005: Aerosol impact on the dynamics and microphysics of deep convective clouds. *Quart. J. Roy. Meteor. Soc.*, **131**, 2639–2663, https://doi.org/10.1256/qj.04.62.

——, N. BenMoshe, and A. Pokrovsky, 2008: Factors determining the impact of aerosols on surface precipitation from clouds: An attempt at classification. *J. Atmos. Sci.*, **65**, 1721–1748, https://doi.org/10.1175/2007JAS2515.1.

——, V. Phillips, N. Benmoshe, and A. Pokrovsky, 2012: The role of small soluble aerosols in the microphysics of deep maritime clouds. *J. Atmos. Sci.*, **69**, 2787–2807, https://doi.org/10.1175/2011JAS3649.1.

Khain, P., J. Shpund, Y. Levi, and A. Khain, 2022: Warm-phase spectral-bin microphysics in ICON: Reasons of sensitivity to aerosols. *Atmos. Res.*, **279**, 106388, https://doi.org/10.1016/j.atmosres.2022.106388.

Köhler, H., 1921: *Zur Kondensation des Wasserdampfes in der Atmosphäre*. Vol. I. kommission hos Cammermeyers boghandel Kristiania, 4 pp.

Koren, I., Y. J. Kaufman, D. Rosenfeld, L. A. Remer, and Y. Rudich, 2005: Aerosol invigoration and restructuring of Atlantic convective clouds. *Geophys. Res. Lett.*, **32**, L14828, https://doi.org/10.1029/2005GL023187.

——, L. A. Remer, O. Altaratz, J. V. Martins, and A. Davidi, 2010: Aerosol-induced changes of convective cloud anvils produce strong climate warming. *Atmos. Chem. Phys.*, **10**, 5001–5010, https://doi.org/10.5194/acp-10-5001-2010.

——, O. Altaratz, L. A. Remer, G. Feingold, J. V. Martins, and R. H. Heiblum, 2012: Aerosol-induced intensification of rain from the tropics to the mid-latitudes. *Nat. Geosci.*, **5**, 118–122, https://doi.org/10.1038/ngeo1364.

Kumjian, M. R., O. P. Prat, K. J. Reimel, M. van Lier-Walqui, and H. C. Morrison, 2022: Dual-polarization radar fingerprints of precipitation physics: A review. *Remote Sens.*, **14**, 3706, https://doi.org/10.3390/rs14153706.

Lakshmanan, V., K. Hondl, C. K. Potvin, and D. Preignitz, 2013: An improved method for estimating radar echo-top height. *Wea. Forecasting*, **28**, 481–488, https://doi.org/10.1175/WAF-D-12-00084.1.

Lance, S., and Coauthors, 2009: Cloud condensation nuclei activity, closure, and droplet growth kinetics of Houston aerosol during the Gulf of Mexico Atmospheric Composition and Climate Study (GoMACCS). *J. Geophys. Res.*, **114**, D00F15, https://doi.org/10.1029/2008JD011699.

Lebo, Z. J., H. Morrison, and J. H. Seinfeld, 2012: Are simulated aerosol-induced effects on deep convective clouds strongly dependent on saturation adjustment? *Atmos. Chem. Phys.*, **12**, 9941–9964, https://doi.org/10.5194/acp-12-9941-2012.

Lerach, D. G., and W. R. Cotton, 2012: Comparing aerosol and low-level moisture influences on supercell tornadogenesis: Three-dimensional idealized simulations. *J. Atmos. Sci.*, **69**, 969–987, https://doi.org/10.1175/JAS-D-11-043.1.

Levy, M. E., and Coauthors, 2013: Measurements of submicron aerosols in Houston, Texas during the 2009 sharp field campaign. *J. Geophys. Res. Atmos.*, **118**, 10 518–10 534, https://doi.org/10.1002/jgrd.50785.

Li, G., Y. Wang, K.-H. Lee, Y. Diao, and R. Zhang, 2009: Impacts of aerosols on the development and precipitation of a mesoscale squall line. *J. Geophys. Res.*, **114**, D17205, https://doi.org/10.1029/2008JD011581.

Li, Z., F. Niu, J. Fan, Y. Liu, D. Rosenfeld, and Y. Ding, 2011: Long-term impacts of aerosols on the vertical development of clouds and precipitation. *Nat. Geosci.*, **4**, 888–894, https://doi.org/10.1038/ngeo1313.

Lindsey, D. T., and M. Fromm, 2008: Evidence of the cloud lifetime effect from wildfire-induced thunderstorms. *Geophys. Res. Lett.*, **35**, L22809, https://doi.org/10.1029/2008GL035680.

Marinescu, P. J., and Coauthors, 2021: Impacts of varying concentrations of cloud condensation nuclei on deep convective cloud updrafts—A multimodel assessment. *J. Atmos. Sci.*, **78**, 1147–1172, https://doi.org/10.1175/JAS-D-20-0200.1.

Matsui, T., H. Masunaga, R. A. Pielke Sr., and W.-K. Tao, 2004: Impact of aerosols and atmospheric thermodynamics on cloud properties within the climate system. *Geophys. Res. Lett.*, **31**, L06109, https://doi.org/10.1029/2003GL019287.

——, B. Dolan, T. Iguchi, S. A. Rutledge, W.-K. Tao, and S. Lang, 2020: Polarimetric radar characteristics of simulated and observed intense convective cores for a midlatitude continental and tropical maritime environment. *J. Hydrometeor.*, **21**, 501–517, https://doi.org/10.1175/JHM-D-19-0185.1.

Miller, R. M., and Coauthors, 2023: Influence of natural and anthropogenic aerosols on cloud base droplet size distributions in clouds over the South China Sea and West Pacific. *Atmos. Chem. Phys.*, **23**, 8959–8977, https://doi.org/10.5194/acp-23-8959-2023.

Morrison, H., 2012: On the robustness of aerosol effects on an idealized supercell storm simulated with a cloud system-resolving model. *Atmos. Chem. Phys.*, **12**, 7689–7705, https://doi.org/10.5194/acp-12-7689-2012.

——, and W. Grabowski, 2011: Cloud-system resolving model simulations of aerosol indirect effects on tropical deep convection and its thermodynamic environment. *Atmos. Chem. Phys.*, **11**, 10 503–10 523, https://doi.org/10.5194/acp-11-10503-2011.

NRC, 2002: *Weather Radar Technology Beyond NEXRAD*. National Academies Press, 81 pp.

Pehl, J., 2023: Influences of the aerosol invigoration effect on radar signatures of deep convection near Houston TX using a bulk statistical framework. M.S. thesis, School of Meteorology, University of Oklahoma, 201 pp., https://shareok.org/bitstreams/2ae7fa26-aa42-4edb-b433-853c33b751b1/download.

Peters, J. M., Z. J. Lebo, D. R. Chavas, and C.-Y. Su, 2023: Entrainment makes pollution more likely to weaken deep convective updrafts than invigorate them. *Geophys. Res. Lett.*, **50**, e2023GL103314, https://doi.org/10.1029/2023GL103314.

Qian, Y., D. Gong, J. Fan, L. R. Leung, R. Bennartz, D. Chen, and W. Wang, 2009: Heavy pollution suppresses light rain in China: Observations and modeling. *J. Geophys. Res.*, **114**, D00K02, https://doi.org/10.1029/2008JD011575.

Randles, C. A., and Coauthors, 2017: The MERRA-2 aerosol reanalysis, 1980 onward. Part I: System description and data assimilation evaluation. *J. Climate*, **30**, 6823–6850, https://doi.org/10.1175/JCLI-D-16-0609.1.

Rosenfeld, D., and I. M. Lensky, 1998: Satellite-based insights into precipitation formation processes in continental and maritime convective clouds. *Bull. Amer. Meteor. Soc.*, **79**, 2457–2476, https://doi.org/10.1175/1520-0477(1998)079<2457:SBIIPF>2.0.CO;2.

——, and W. L. Woodley, 2000: Deep convective clouds with sustained supercooled liquid water down to −37.5°C. *Nature*, **405**, 440–442, https://doi.org/10.1038/35013030.

——, U. Lohmann, G. B. Raga, C. D. O'Dowd, M. Kulmala, S. Fuzzi, A. Reissell, and M. Andreae, 2008: Flood or drought: How do aerosols affect precipitation? *Science*, **321**, 1309–1313, https://doi.org/10.1126/science.1160606.

Ryzhkov, A., P. Zhang, H. Reeves, M. Kumjian, T. Tschallener, S. Trömel, and C. Simmer, 2016: Quasi-vertical profiles—A new way to look at polarimetric radar data. *J. Atmos. Oceanic Technol.*, **33**, 551–562, https://doi.org/10.1175/JTECH-D-15-0020.1.

Scott, D. W., 2015: *Multivariate Density Estimation: Theory, Practice, and Visualization*. John Wiley and Sons, 350 pp.

Seifert, A., and K. D. Beheng, 2006: A two-moment cloud microphysics parameterization for mixed-phase clouds. Part 2: Maritime vs. continental deep convective storms. *Meteor. Atmos. Phys.*, **92**, 67–82, https://doi.org/10.1007/s00703-005-0113-3.

Shepherd, J. M., and S. J. Burian, 2003: Detection of urban-induced rainfall anomalies in a major coastal city. *Earth Interact.*, **7**, https://doi.org/10.1175/1087-3562(2003)007<0001:DOUIRA>2.0.CO;2.

Sherwood, S. C., 2002: Aerosols and ice particle size in tropical cumulonimbus. *J. Climate*, **15**, 1051–1063, https://doi.org/10.1175/1520-0442(2002)015<1051:AAIPSI>2.0.CO;2.

——, V. T. J. Phillips, and J. S. Wettlaufer, 2006: Small ice crystals and the climatology of lightning. *Geophys. Res. Lett.*, **33**, L05804, https://doi.org/10.1029/2005GL025242.

Tao, W.-K., X. Li, A. Khain, T. Matsui, S. Lang, and J. Simpson, 2007: Role of atmospheric aerosol concentration on deep convective precipitation: Cloud-resolving model simulations. *J. Geophys. Res.*, **112**, D24S18, https://doi.org/10.1029/2007JD008728.

——, J.-P. Chen, Z. Li, C. Wang, and C. Zhang, 2012: Impact of aerosols on convective clouds and precipitation. *Rev. Geophys.*, **50**, RG2001, https://doi.org/10.1029/2011RG000369.

Taszarek, M., N. Pilguj, J. T. Allen, V. Gensini, H. E. Brooks, and P. Szuster, 2021: Comparison of convective parameters derived from ERA5 and MERRA-2 with rawinsonde data over Europe and North America. *J. Climate*, **34**, 3211–3237, https://doi.org/10.1175/JCLI-D-20-0484.1.

Twomey, S., 1977: The influence of pollution on the shortwave albedo of clouds. *J. Atmos. Sci.*, **34**, 1149–1152, https://doi.org/10.1175/1520-0469(1977)034<1149:TIOPOT>2.0.CO;2.

Varble, A., 2018: Erroneous attribution of deep convective invigoration to aerosol concentration. *J. Atmos. Sci.*, **75**, 1351–1368, https://doi.org/10.1175/JAS-D-17-0217.1.

——, A. L. Igel, H. Morrison, W. W. Grabowski, and Z. J. Lebo, 2023: Opinion: A critical evaluation of the evidence for aerosol invigoration of deep convection. *Atmos. Chem. Phys.*, **23**, 13 791–13 808, https://doi.org/10.5194/acp-23-13791-2023.

Veals, P. G., A. C. Varble, J. O. H. Russell, J. C. Hardin, and E. J. Zipser, 2022: Indications of a decrease in the depth of deep convective cores with increasing aerosol concentration during the CACTI campaign. *J. Atmos. Sci.*, **79**, 705–722, https://doi.org/10.1175/JAS-D-21-0119.1.

Wang, C., 2005: A modeling study of the response of tropical deep convection to the increase of cloud condensation nuclei concentration: 1. Dynamics and microphysics. *J. Geophys. Res.*, **110**, D21211, https://doi.org/10.1029/2004JD005720.

Wang, H., and Coauthors, 2013: Sensitivity of remote aerosol distributions to representation of cloud–aerosol interactions in a global climate model. *Geosci. Model Dev.*, **6**, 765–782, https://doi.org/10.5194/gmd-6-765-2013.

White, B., E. Gryspeerdt, P. Stier, H. Morrison, G. Thompson, and Z. Kipling, 2017: Uncertainty from the choice of microphysics scheme in convection-permitting models significantly exceeds aerosol effects. *Atmos. Chem. Phys.*, **17**, 12 145–12 175, https://doi.org/10.5194/acp-17-12145-2017.

Williams, E., D. Rosenfeld, N. Madden, C. Labrada, J. Gerlach, and L. Atkinson, 1999: The role of boundary layer aerosol in the vertical development of precipitation and electrification: Another look at the contrast between lightning over land and over ocean. *11th Int. Conf. on Atmospheric Electricity*, Guntersville, AL, National Aeronautics and Space Administration, 754–757, https://ntrs.nasa.gov/citations/19990108601.

Yuter, S. E., and R. A. Houze Jr., 1995: Three-dimensional kinematic and microphysical evolution of Florida cumulonimbus. Part II: Frequency distributions of vertical velocity, reflectivity, and differential reflectivity. *Mon. Wea. Rev.*, **123**, 1941–1963, https://doi.org/10.1175/1520-0493(1995)123<1941:TDKAME>2.0.CO;2.

Zamora, L. M., and R. A. Kahn, 2020: Saharan dust aerosols change deep convective cloud prevalence, possibly by inhibiting marine new particle formation. *J. Climate*, **33**, 9467–9480, https://doi.org/10.1175/JCLI-D-20-0083.1.

Zang, L., D. Rosenfeld, Z. Pan, F. Mao, Y. Zhu, X. Lu, and W. Gong, 2023: Observing aerosol primary convective invigoration and its meteorological feedback. *Geophys. Res. Lett.*, **50**, e2023GL104151, https://doi.org/10.1029/2023GL104151.

Zhang, Y., J. Fan, Z. Li, and D. Rosenfeld, 2021: Impacts of cloud microphysics parameterizations on simulated aerosol–cloud interactions for deep convective clouds over Houston. *Atmos. Chem. Phys.*, **21**, 2363–2381, https://doi.org/10.5194/acp-21-2363-2021.